Multiscale model for microstructure evolution in multiphase materials: Application to the growth of isolated inclusions in presence of elasticity

Danny Perez* and Laurent J. Lewis†
Département de physique et Regroupement Québécois sur les Matériaux de Pointe (RQMP), Université de Montréal, C. P. 6128 Succursale Centre-Ville, Montréal (Québec), Canada H3C 3J7
(Received 25 May 2006; published 26 September 2006)

We present a multiscale model based on the classical lattice time-dependent density-functional theory to study microstructure evolution in multiphase systems. As a first test of the method, we study the static and dynamic properties of isolated inclusions. Three cases are explored: elastically homogeneous systems, elastically inhomogeneous systems with soft inclusions, and elastically inhomogeneous systems with hard inclusions. The equilibrium properties of inclusions are shown to be consistent with previous results: both homogeneous and hard inclusions adopt a circular shape independent of their size, whereas soft inclusions are circular below a critical radius and elliptic above. In all cases, the Gibbs-Thomson relation is obeyed, except for a change in the prefactor at the critical radius in soft inclusions. Under growth conditions, homogeneous inclusions exhibit a Mullins-Sekerka shape instability [W. Mullins and R. Sekerka, J. Appl. Phys. **34**, 323 (1963)], whereas in inhomogeneous systems, the growth of perturbations follows the Leo-Sekerka model [P. Leo and R. Sekerka, Acta Metall. **37**, 3139 (1989)]. For soft inclusions, the mode instability regime is gradually replaced by a tip-growing mechanism, which leads to stable, strongly out-of-equilibrium shapes even at very low supersaturation. This mechanism is shown to significantly affect the growth dynamics of soft inclusions, whereas dynamical corrections to the growth rates are negligible in homogeneous and hard inclusions. Finally, due to its microscopic formulation, the model is shown to automatically take into account phenomena caused by the presence of the underlying discrete lattice: anisotropy of the interfacial energy, anisotropy of the kinetics, and preferential excitation of shape perturbations commensurate with the rotational symmetry of the lattice.

DOI: 10.1103/PhysRevE.74.031609 PACS number(s): 81.10.−h, 61.66.Dk, 61.72.Qq, 64.75.+g

I. INTRODUCTION

It is well known that many macroscopic properties of materials, such as tensile resistance, electric conductivity, ductility, etc., are directly related to the microscale structure. However, the microstructure is a dynamical entity: it evolves continuously inducing changes in the properties for which the material was initially designed. It is thus of prime importance to understand the forces driving microstructural evolution in order to tailor materials that are able to maintain their properties over long time scales. However, this task has proven formidable because, in "real-life" materials, the observed microstructure is the result of a delicate balance between many competing physical processes. For example, in the common case of two-phase materials, which is the subject of this paper, the microstructure consists of inclusions embedded within a matrix. In general, the inclusions and the matrix will have different physical properties (elastic constants, diffusion constants, lattice parameters, etc.) so that the free energy (which is minimized during microstructural evolution) will have chemical, interfacial, and elastic components. In order to study the formation and evolution of the microstructure, a description of each of these components is required.

The first step toward a complete understanding of the evolution of the microstructure is to identify the equilibrium state toward which simple systems proceed. For two-phase systems without lattice misfit, the shape of an isolated inclusion is strictly driven by interfacial energy considerations and can thus be obtained simply by using a Wolff construction. However, in the presence of lattice misfits, the situation is much more complicated. Indeed, the problem of finding the free-energy-minimizing configurations is an old one (see Ref. [1] for a recent review). The basic behavior of these systems is now well established in the simplest cases. For example, in the case of inhomogeneous but isotropic elasticity and isotropic interface energy, isolated spherical hard inclusions are stable for all sizes, i.e., the equilibrium shape of the inclusions is not affected by the elastic contributions to the free energy [2]. However, if the inclusions are softer than the matrix, the spherical shape is only stable at small radius; at large radius the symmetry is broken and the equilibrium shape becomes increasingly elliptic [2].

Although the structural behavior of isolated inclusions is now well known, much less is known about the relation between their structure and their coarsening behavior. (A notable exception is the recent work of Thornton *et al.* [3] and of Li *et al.* [4] concerning homogeneous and inhomogeneous, anisotropic elasticity with isotropic surface energy.) In order to make this connection, the effect of shape changes on the solute concentration, or equivalently on the chemical potential, inside and around the inclusions has to be studied. This information, taking the form of a so-called Gibbs-Thomson relation, is essential to understanding the coarsening dynamics of a system of diffusively interacting inclusions, since it dictates the rate at which a given inclusion of

*Electronic address: danny.perez@umontreal.ca
†Electronic address: Laurent.Lewis@UMontreal.CA

a particular size (and shape) grows or dissolves. However, for the knowledge of the equilibrium properties to be really useful, it must be the case that, at any given time, the microstructure is close to equilibrium. Therefore, the effect of finite growth rates on the coarsening behavior has to be assessed. The morphological consequences of finite growth rates on the inclusions have also been thoroughly investigated [5–9], but the relation between shape perturbations and chemical potentials and, hence, coarsening behavior, is much less understood. In order to assess the importance of dynamical effects, it is necessary to study the effect of the dynamical corrections on the Gibbs-Thomson relation.

In this paper, we study the equilibrium and dynamical properties of isolated inclusions in the case of homogeneous and inhomogeneous, isotropic elasticity under varying growth rate, and infer the consequences of dynamical corrections on the coarsening behavior of systems of inclusions. This is achieved using a two-dimensional, multiscale model based on the classical lattice time-dependent density-functional theory (TDDFT) [10,11]. The focus of this work is twofold: first, we validate the methodology by comparing our observations to theoretical models or numerical simulations (mainly concerning morphological aspects); second, we present results for the connection between morphology and the coarsening behavior of inclusions.

Anticipating our results, we observe that the classical Gibbs-Thomson behavior is obeyed in homogeneous circular inclusions, as expected. Under imposed growth, shape instabilities develop and, for small amplitudes, their behavior is consistent with the predictions of the Mullins-Sekerka theory [5]. The microscopic resolution of our model enables us to identify an efficient excitation process for modes with the same rotational symmetry as that of the lattice. The impact of growth on the chemical potentials of the inclusions is then characterized, and we show that dynamical corrections to the coarsening behavior are small. Hard inclusions are observed to also exhibit the Gibbs-Thomson behavior. Elasticity is shown to have a stabilizing effect against shape perturbation growth, in agreement with the theory of Leo and Sekerka [6]. In this case also, dynamical corrections to the growth dynamics are small. Finally, for soft inclusions, we observe the expected equilibrium transition between circular and elliptic shapes and quantify its effect on the chemical potentials of the inclusions. Soft inclusions are found to be extremely sensitive to growth conditions: strongly out of equilibrium shapes form and survive even at very low supersaturation. Although the behavior predicted by the Leo and Sekerka model is observed at small radii, we find that an elastically induced growth mechanism favoring the growth of tips dominates the evolution at larger sizes. The effect of dynamical corrections on the growth dynamics is shown to be significant in this case because of the important morphological changes induced by finite growth rates.

The paper is organized as follows. In Sec. II, we describe the model, its multiscale generalization, and the methodology used to solve the relevant system of equations. In Sec. III, we present the results of our calculations for homogeneous, hard and soft inclusions, respectively. In each case, we describe the equilibrium properties of isolated inclusions, then investigate how these properties are affected by finite growth rates and examine the importance of these corrections on the coarsening rate. Finally, in Sec. IV, we discuss the implication of our results for the description of the coarsening kinetics of a collection of inclusions.

II. METHODOLOGY

The microstructural evolution of a multiphase material in presence of elastic misfits is an intrinsically multiscale problem: on the one hand, at moderate temperatures, the interphase boundary is only a few atomic-layers thick so that mechanical and chemical properties of the material may vary strongly on a nanometer length scale; on the other hand, the elastic strain field caused by the presence of the inclusion is very long ranged. Adding to the difficulty is the coupling between thermodynamics, diffusion, and elasticity: elastic stresses can affect the local chemical potentials inside the material, thus causing diffusion fluxes that modify the elastic response of the system, and so on.

However, most models proposed thus far to study two-phase systems with elastic misfits are essentially single scale—macroscopic sharp-interface models [3,12–14], mesoscopic diffuse interface models (also known as phase-field models) [15–17], or microscopic Monte Carlo models [18–21]—and thus suffer from some drawbacks. First, sharp-interface models assume the interfaces to be infinitely thin and structure less, thus lacking internal length scales. These have to be introduced *a posteriori* if scale-dependent effects (such as shape transitions as a function of size) need to be taken into account. Also, interphase boundary conditions have to be devised artificially in order to introduce proper physics into the models (e.g., solute concentration vs interface curvature or strain relations must be specified) which, for simplicity, often rely on some local equilibrium assumption. Relevant physical parameters (diffusion constant, elastic constants, etc.) are also needed as input. Finally, the models do not easily allow for topological changes in the microstructure (merging of inclusions for example).

Diffuse interface methods, for their part, assume that all physical properties of the microstructure vary smoothly on the scale of the grid used in the calculations. However, in typical two-phase microstructures, the interfaces are a only few nanometers thick. This imposes strong limitations on the possible grid sizes if quantitative results are sought. Even if this requirement is somewhat relaxed, the grid size still needs to be smaller than any other length scale in the system. In the presence of elastic effects, this constraint can be severe [22]. Furthermore, these models need external input for the thermodynamic (e.g., bulk free energy vs concentration, chemical potential vs strain), elastic (e.g., elastic constants), and diffusion (e.g., temperature or concentration dependence of the diffusion rates) properties of the material, and the coupling between these properties. Despite these limitations, macro- and mesoscopic simulations (MMS) are extremely powerful tools since they enable very large systems, composed of many inclusions, to be studied over long durations.

At the other end of the spectrum, Monte Carlo models are formulated directly on the atomic scale, the natural scale for describing interphase boundaries. Furthermore, the thermo-

dynamic and elastic properties are implicitly obtained from the microscopic description of the interactions between atoms. This microscopic description also allows one to specify the microscopic diffusion processes and to automatically take the composition dependence of the diffusion rates into account. However, these nice features come at a very high computational cost, so that such calculations are restricted to small systems over short time scales. Since elastic interactions are long ranged and their effects usually predominate over interface effects only in the late stages of the coarsening process, Monte Carlo simulations are seldom used in this context. The causes of this inefficiency compared to MMS are fourfold. First, Monte Carlo moves are essentially local in nature so that a large number is required to significantly alter the microstructure, whereas for MMS, the update steps are global. Second, except at very low temperature, many of the moves are, in fact, thermal "noise;" thus, although on average they tend to relax the microstructure, on an individual basis they do not contribute significantly to the relaxation process. These thermal fluctuations are already averaged out in MMS, so that every step directly contributes to the structural evolution. Third, the time step is roughly constant throughout the simulation, independent of the time scale on which the microstructure evolves; in constrast, the time step for MMS can be adjusted dynamically. Finally, the number of degrees of freedom required to describe the microstructure is very large since all atomic sites are explicitly taken into account, whereas in MMS one degree of freedom represents a large number of atomic sites.

One way around this efficiency problem is to consider equations for the evolution of the *average* occupation state of each lattice site. In this way, thermal fluctuations can be integrated out and global updates of the system become possible. Even if such equations cannot be derived exactly, several approximation schemes have been proposed in recent years to simulate phase separation without elastic misfit (see Refs. [11,23,24], for example). Although these approaches are able to bypass the first three drawbacks of the Monte Carlo method, the problem of the large number of degrees of freedom remains. Here, we propose to solve this last point by using a multiscale generalization of one of the aforementioned schemes, namely, the TDDFT of Fisher and collaborators [11]. We also propose an extension of this framework to include the effect of elastic misfits. The remaining part of this section will be organized as follows: first, we outline the derivation of the TDDFT equations and describe how elastic effects can be included within the model; second, the multiscale generalization of the microscopic model is presented; finally, we give a brief description of the algorithmic tools used in our implementation of the model.

A. The TDDFT formalism

We begin by deriving the main equations of TDDFT. Since a detailed description of the theory is already available in the literature (see Ref. [11], and references therein), only the main steps are outlined here for completeness. Consider a system of interacting particles on a lattice. The state of the lattice sites can be described by an ensemble of occupation numbers n_i^α for α-type particles at site i. Assuming that each site can be occupied by only one particle (n_i^α equals either 0 or 1), the dynamics of the system can formally by described by the following master equation for the probability to find the system in the configuration $\mathbf{n}=\{n_i^\alpha\}$ at time t:

$$\frac{dP(\mathbf{n},t)}{dt} = \frac{1}{2}\sum_{i,j\in nn(i)} [w_{i,j}(\tilde{\mathbf{n}})P(\tilde{\mathbf{n}},\mathbf{t}) - w_{i,j}(\mathbf{n})P(\mathbf{n},t)]. \quad (1)$$

Here, it is assumed that a configuration evolves in time through successive exchanges of nearest-neighbors particles [$nn(i)$ denotes the set of nearest neighbors of site i]. These exchanges proceed at rate $w_{i,j}(\mathbf{n})$; $\tilde{\mathbf{n}}$ represents a configuration that differs from $\mathbf{n}$ only by the exchange of the occupation numbers of sites i and j. From Eq. (1), a local master equation describing the dynamics of the *average* occupation numbers $p_i^\alpha=\langle n_i^\alpha\rangle_t$ [where $\langle\rangle_t$ denotes an average with respect to the distribution $P(\mathbf{n},\mathbf{t})$] is obtained

$$\frac{dp_i^\alpha}{dt} = \sum_{j\in nn(i),\beta} \langle J_{i,j}^{\beta,\alpha}\rangle_t - \langle J_{i,j}^{\alpha,\beta}\rangle_t, \quad (2)$$

with the diffusion fluxes defined as

$$J_{i,j}^{\beta,\alpha}(\mathbf{n}) = n_i^\beta n_j^\alpha w_{i,j}(\mathbf{n}). \quad (3)$$

The problem now is to evaluate the average diffusion fluxes. The main assumption of TDDFT is that the full nonequilibrium distribution function $P(\mathbf{n},t)$ can be approximated by the local equilibrium distribution function $P^{\mathrm{loc}}(\mathbf{n},t)$ of the system under an external, site-dependent field h_i^α,

$$P^{\mathrm{loc}}(\mathbf{n},t) = \frac{1}{Z(t)}\exp\left\{-\frac{1}{k_BT}\left[H(\mathbf{n}) + \sum_{i,\alpha} h_i^\alpha n_i^\alpha\right]\right\}, \quad (4)$$

where H is the Hamiltonian of the system and $Z(t)$ is such that $\Sigma_{\mathbf{n}}P^{\mathrm{loc}}(\mathbf{n},t)=1$. The problem of computing the nonequilibrium distribution function in configuration space is now replaced by that of determining the $\{h_i^\alpha\}$ in real space. This is achieved by requiring consistency between $P^{\mathrm{loc}}(\mathbf{n},t)$ and the $\{p_i^\alpha(t)\}$. The idea behind this assumption is that high-order correlations should relax rapidly compared to the site occupation averages; hence, after a short initial transient, the high-order correlation functions should take values close to the ones they would relax to if the average occupations were kept constant by some external constraint. The validity of this assumption has been confirmed by Chen [23] who has shown that the dynamics of a system where pair-correlation functions are allowed to evolve following their own equations of motion is quantitatively very similar to that of a system where instantaneous equilibrium of the pair correlation functions relative to the site occupation averages is assumed. Furthermore, it was shown [25] that the TDDFT approach yields results in excellent agreement with direct Monte Carlo simulation in cases where the exact free energy functional is available.

Formally, self-consistency can be achieved by requiring that the grand canonical potential of the system under the external field be a minimum with respect to the average occupations, i.e., the h_i^α are such that

$$\frac{d}{d\mathbf{p}}\Omega(\mathbf{p}) = \frac{d}{d\mathbf{p}}\left[\sum_{i,\alpha}(h_i^\alpha - \mu_{\text{tot}}^\alpha)p_i^\alpha + F(\mathbf{p})\right] = 0, \tag{5}$$

where $\mathbf{p}=\{p_i^\alpha\}$, μ_{tot}^α is the global chemical potential of species α, and $F(\mathbf{p})$ is the free-energy functional of the system. From this last equation, it is now clear that the local fields are proportional to the local chemical potentials

$$h_i^\alpha = \mu_{\text{tot}}^\alpha - \frac{\partial F}{\partial p_i^\alpha} = \mu_{\text{tot}}^\alpha - \mu_i^\alpha. \tag{6}$$

To complete the evaluation of the fields, one must specify a free-energy functional. In our case, we opted for a simple mean-field (or Bragg-Williams) approximation, which, even if it usually cannot reproduce experimentally observed phase diagrams in a quantitative manner, gives a qualitatively correct description of the phase separation process. This functional can be written as follows

$$F(\mathbf{p}) = E(\mathbf{p}) - TS(\mathbf{p}) = \frac{1}{2}\sum_{i,j\in nn(i),\alpha,\beta} V_{i,j}^{\alpha,\beta} p_i^\alpha p_j^\beta + k_B T\sum_{i,\alpha} p_i^\alpha \ln p_i^\alpha, \tag{7}$$

with $V_{i,j}^{\alpha,\beta}$ the interaction energy between atom α at site i and atom β at site j.

Other assumptions are required in order to obtain a tractable form for the average diffusion fluxes. First, it is assumed that configuration changes can only occur by vacancy diffusion to a nearest-neighbor site (vacancy-exchange mechanism). Second, these exchanges occur at a rate given by

$$w_{i,j}^\alpha = \nu_0 e^{E_i^\alpha/k_B T}, \tag{8}$$

where E_i^α is the energy of an α-type atom at site i and ν_0 is a trial frequency. This assumes that the saddle point energy is zero in every configuration.

Combining this last result with Eqs. (3) and (4), we obtain a very simple form for the local master equation [Eq. (2)]

$$\frac{dp_i^\alpha}{dt} = \sum_{j\in nn(i)} M_{i,j}(t)[\mathcal{A}_j^\alpha(t) - \mathcal{A}_i^\alpha(t)], \tag{9}$$

with mobility $M_{i,j}(t) = \langle p_i^{\text{vacancy}}(t)p_j^{\text{vacancy}}(t)\rangle_t \simeq p_i^{\text{vacancy}}(t)p_j^{\text{vacancy}}(t)$ and activity $\mathcal{A}_i^\alpha(t) = e^{-h_i^\alpha(t)/k_B T}$. This equation is a generalized Fick's law, where occupation probabilities diffuse from regions of high activity (and, hence, high chemical potential) to regions of low activity. It can be shown that this equation of motion leads to a continuous decrease of the free-energy evaluated through Eq. (7) and, hence, that a stationary state of Eq. (9) corresponds to a free-energy minimum. Even if TDDFT is a mean-field formalism, this shows that it yields an evolution that is consistent with the equilibrium statistics specified by the free-energy functional. Furthermore, as previously mentioned, TDDFT and Monte Carlo results were shown to be nearly identical for both equilibrium and dynamical quantities for cases where the exact energy functional is known [25]. Thus, in the present case, we cannot expect quantitative agreement with Monte Carlo simulations. However, since we are not seeking quantitative results, but rather insights into the basic physical behavior, we expect this simple approximation to be adequate. The use of higher-order approximations of the free energy will be the subject of future work.

B. TDDFT with elastic misfit

In the formalism described above, the atoms are constrained on a rigid lattice. Thus, the effect of an elastic misfit cannot be accounted for. One way to introduce elastic relaxation effects is to allow the interaction energies in Eq. (7) to depend on the positions of the atoms. For simplicity, we opted for a simple harmonic potential

$$V_{i,j}^{\alpha,\beta} = k^{\alpha,\beta}(r_{i,j} - \sigma^{\alpha,\beta})^2 - \epsilon^{\alpha,\beta}, \tag{10}$$

where $r_{i,j}=|\vec{r}_i-\vec{r}_j|$. The *average* positions $\vec{r}_i$ are then obtained by requiring that they minimize Ω [or equivalently the energy in Eq. (7)], i.e.,

$$\frac{d}{d\mathbf{r}}\Omega(\mathbf{p},\mathbf{r}) = \frac{d}{d\mathbf{r}}\left[\sum_{i,\alpha}(h_i^\alpha - \mu_{\text{tot}}^\alpha)p_\mathbf{l}^\alpha + F(\mathbf{p},\mathbf{r})\right] = 0 = \frac{d}{d\mathbf{r}}E(\mathbf{p},\mathbf{r}) = 0. \tag{11}$$

In this way, if we select different values of the lattice parameter σ for the interaction between different species, a lattice mismatch is introduced. Furthermore, if we select different values of the stiffness k, an elastic inhomogeneity results. Likewise, the strength of the driving force for the phase separation can be tuned according to ϵ. Note that for nearest-neighbor, two-body interactions, such as the ones used here, the elastic constants are always isotropic.

Concerning the accuracy of this formulation, two remarks are in order. First, this procedure completely neglects local relaxation effects, i.e., the same displacement field is used to compute, say, E_i^α and E_i^β. This somewhat overestimates the effect of the strain, since local relaxation is expected to be most effective in severely strained configurations. Second, in the present approach, elasticity is introduced at the mean-field level since atoms interact with the free-energy-minimizing displacement field, not the displacement field corresponding to a particular microscopic configuration. These two limitations are not expected to be severe in the case of a system composed of a set of almost pure inclusions embedded in an almost pure matrix (typical of the microstructures produced during phase separation processes), since every microscopic configuration that has a significant probability of being observed will have a displacement field very similar to the free-energy minimizing one. Thus, these approximations are expected to yield very good results when used in a phase separation context.

Finally, we assume that the neighbors of an atomic site do not change during the course of a simulation, i.e., elastic coherency is enforced and the contribution of plastic effects is excluded.

C. Multiscale generalization

The TDDFT model described in Sec. II A is essentially microscopic in nature since every lattice site is explicitly

taken into account. This imposes severe constraints on the system sizes that can be studied. In order to alleviate this limitation, we propose a multiscale generalization of TDDFT where the number of degrees of freedom can be dynamically adjusted as the calculation proceeds. In the following, we describe first the coarse-graining procedure of the TDDFT local master equation [Eq. (9)], then the elastic equilibrium equation [Eq. (11)].

1. Coarse graining of the TDDFT equations

As discussed earlier, a typical microstructure observed in phase-separating systems consists of well-defined inclusions embedded in a matrix. Within each of these structures, the average occupation field varies very slowly. The only rapid changes occur close to the interphase boundaries. Thus, atomic resolution is, in principle, only needed close to the interfaces, whereas lattice sites located far from these interfaces can collectively be described using fewer degrees of freedom. To achieve this, two ingredients are required: (i) a coarse-grainable representation of the average occupation field and (ii) a method to solve Eq. (9) in this representation.

For (i), we proceed as follows. First, we select a set of atomic sites whose average occupations are representative of their neighborhoods (the procedure used to build this set will be described in Sec. II D); those sites will be referred to as *representative sites*. When needed, the average occupation of nonrepresentative sites are obtained by a Laplace interpolation [26] defined as follows. Let $\mathbf{x}$ be a point in space; the Laplace interpolant for a general scalar function $f(\mathbf{x})$ is

$$f^I(\mathbf{x}) = \sum_{i=1}^{N_{\text{rep}}} \phi_i(\mathbf{x}) f_i, \tag{12}$$

where N_{rep} is the number of representative sites, f_i is the (known) value of the function f at representative site i, and $\phi_i(\mathbf{x})$ is the value of the Laplace shape function of site i evaluated at $\mathbf{x}$. We now consider a Voronoï tesselation of space using the representative site and point $\mathbf{x}$. The shape function can then be written as

$$\phi_i(\mathbf{x}) = \frac{s_i(\mathbf{x})}{\sum_{j=1}^{N_{\text{rep}}} s_j(\mathbf{x})}, \quad s_j(\mathbf{x}) = \frac{m[t_j(\mathbf{x})]}{d_j(\mathbf{x})}, \tag{13}$$

with $d_j(\mathbf{x})$ the distance between $\mathbf{x}$ and the representative site j, and $m[t_j(\mathbf{x})]$ a measure of the common facet (length in two-dimensions and area in three dimensions) between the Voronoï cells of site j and of point $\mathbf{x}$; if the two cells do not share facets, $m[t_j(\mathbf{x})]=0$. A review of the properties of this interpolant can be found in Ref. [26].

The Voronoï tesselation of space using the representative sites provides a definition of the "neighborhood" of a representative site: all lattice sites found within the Voronoï cell of a given representative site belong to its neighborhood. The last step is to reformulate Eq. (9) in terms of the average occupations of the neighborhoods instead of the average occupations of the lattice sites. Concerning point (ii), the key is to realize that this equation is essentially a diffusion equation for the occupation probabilities, with a probability flux between adjacent sites proportional to the activity difference between the two sites. Since the total occupation probabilities are conserved, this can easily be translated into a coarse-grained representation by using the finite-volume method. The time derivative of Eq. (9) is then written in terms of the diffusion fluxes crossing each facet of the Voronoï cells of the representative sites; on an arbitrary grid, Eq. (9) becomes

$$\frac{dp_i^\alpha}{dt} = \sum_{j \in nn(i)} M_{i,j}(t)[\mathcal{A}_j^\alpha(t) - \mathcal{A}_i^\alpha(t)] \frac{b_{i,j}}{d_{i,j} N_i}, \tag{14}$$

with $d_{i,j}$ the distance (in lattice constants) between representative sites i and j, N_i the number of lattice sites inside the Voronoï cell of representative site i, and $b_{i,j}$ the number of nearest-neighbor links intersected by the common facet of Voronoï cells i and j. For a rigorous derivation of such a finite-volume scheme on unstructured grids, one may consult Refs. [26,27]. One nice feature of this coarse-graining scheme is that Eq. (14) reduces exactly to Eq. (9) as the grid is refined to the original lattice since, in this case, $d_{i,j}=1$, $N_i=1$, and $b_{i,j}=1$. Thus, this formulation allows for seamless changes in the resolution of the TDDFT calculations, from the micro- to the mesoscale. The only requirement is that the average occupation field varies slowly on the scale of the distance between representative sites. Since the variations in this field are very sharp and well localized, this is not a serious limitation.

2. Coarse graining of the elastic equilibrium equations

Since the activities in Eq. (14) also depend on the average displacement of the atoms in the neighborhood of the representative sites, the elastic equilibrium equation [Eq. (11)] is also required to be coarse grained. The formulation is naturally provided by the quasicontinuum method (QCM) of Tadmor and collaborators [28] (see Ref. [29] for a recent review of the method and its applications). Since its introduction, the QCM has proven to be very effective in providing a multiscale description of the micro- and mesoscale elastic behavior of materials using only interatomic potentials as input. It was successfully applied to simulations of fracture [30], nanoindentation [31], and failure of carbon nanotubes under tension [32], to name only a few examples.

We give here a rapid overview of its most important aspects. The first step is to reduce the number of degrees of freedom required to describe the displacement field. Again here, we express the average displacement field at every lattice site in terms of the average displacements of the representative sites using the Laplace interpolation scheme described above. Note that this departs from the standard QCM procedure, where linear shape functions defined on triangular elements are used. In our case, it is simpler to use the same interpolation scheme for both occupations and displacements. Next, we write a coarse-grained energy functional for the complete system as a function only of the representative site displacements. For this purpose, we make use of the so-called nonlocal energy-based formulation of the QCM [29]. In this formulation, the coarse-grained energy can be written as a sum over the energy of the representative sites

$$E^{\text{tot,QCM}} = \sum_{i=1}^{N_{\text{rep}}} N_i E_i^{int}, \tag{15}$$

where E_i^{int} is the energy of site i evaluated using Eqs. (7) and (10) with the Laplace-interpolated average displacements. The last step is to minimize the coarse-grained energy with respect to the average displacements of the representative atoms. This can be carried out using any standard minimization method. In this case also, the nonlocal QCM formalism reduces exactly to the original microscopic model when the grid is refined to the original lattice; thus, scale-dependent effects and nonlinearities are fully taken into account.

D. Choice of representative sites

In Sec. II C 1 and II C 2, it was shown how a coarse-grainable formulation of our model can be obtained, based on the assumption that a representation of the relevant fields can be constructed from the values that these fields take on a subset of all lattice sites (the representative sites). In this section, the question of how this subset is chosen is addressed. In principle, choosing a representative set for the TDDFT equations is an easy task: atomic resolution is required only in the vicinity of the interphase boundaries, whereas a coarser grid can be used elsewhere. It turns out that this strategy is also appropriate for the elastic equilibrium equation of the QMC since it adequately captures the changes in elastic properties between the different phases. Furthermore, rapid changes in the displacement field also tend to occur near the interfaces. For example, in the case of a circular inclusion in an elastically isotropic and homogeneous matrix, the radial displacement component increases linearly with the distance to the center of the inclusion until the interface is reached, where it abruptly begins to decrease [33]. Although it is true that a more aggressive optimization could be achieved by choosing different sets for the TDDFT and the QCM, the performance gain would probably be more then offset by the increased complexity of the code. Thus, only a common representative set will be used here.

To facilitate both creation and management, a few constraints on the composition of the representative set are enforced. First, only four levels of coarsening are allowed ($L=0,1,2,3$); in a region of level L of a D-dimensional lattice, one out of every 2^{DL} sites is included in the representative set. Second, the representative set forms a semistructured grid, meaning that the level-L representative set is a subset of the level-L' representative set for $L>L'$. Finally, the local coarsening level is obtained from the distance d_i to the closest interphase boundary by $L=\min(\lfloor d_i/d_l \rfloor, 3)$. In the calculations presented below, we used $d_l=7a_0$, where a_0 is the lattice parameter. The limit imposed on the number of coarsening levels ensures a smooth and rapid convergence of the TDDFT and QCM equations. (A very large difference in the volumes of the representative cells generally causes poor convergence.)

Because the microstructure evolves in time, the adequacy of the representative set is checked periodically, and is automatically corrected as necessary. An example of the Voronoï cells around the representative sites for the case of a single circular inclusion within a homogeneous matrix in two dimensions is show in Fig. 1. One can easily appreciate the reduction in the number of degrees of freedom resulting from the multiscale formalism presented here.

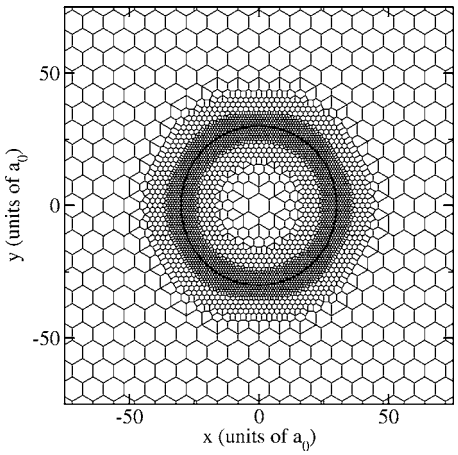

FIG. 1. Voronoï cells around the representative sites for a single inclusion embedded within an otherwise homogeneous matrix in two dimensions. The contour of the inclusion is shown by the thick black line.

E. Implementation details

As a first implementation of this method, we chose to work in two dimensions. We examine the case of a binary alloy with vacancies (ABv alloy), but ternary alloys could just as easily be simulated. The integration of the TDDFT equations [Eq. (14)] are carried out implicitly using the order 5 backward differentiation formulas of Gear [34]. Every implicit integration step requires the solution of a nonlinear problem. This is obtained by a Newton-Krylov method [35] using the stabilized biconjugate gradient algorithm without preconditioning [36]. Since it is readily available, the exact Jacobian is used in the non-linear solution. This elaborate scheme is necessary because the TDDFT equations for our system are very stiff, so that simpler explicit methods are limited to extremely small time steps for stability reasons. To minimize the QMC energy functional Eq. (15) (and hence the free energy) with respect to the site displacements, we use the conjugate-gradient algorithm [37] on the QCM forces using the exact Hessian matrix.

III. RESULTS

A. Simulation setup

In the following, we present our results for the growth of isolated inclusions in elastically inhomogeneous systems with elastic misfit. In all calculations, the inclusion is rich in B-type atoms, whereas the matrix is rich in A-type atoms. All results are reported in dimensionless, reduced units, relative to a stress-free pure A phase: lattice parameter for length (a_0), interaction energy between nearest-neighbors for energy (ϵ), and inverse trial frequency for time (τ_0). In those units, the parameters of the inter-atomic potential Eq. (10)

were chosen to be: $\epsilon_{AA}=\epsilon_{BB}=\epsilon$, $\epsilon_{AB}=0.7\epsilon$ and $\sigma_{AA}=\sigma_{AB}=a_0$, $\sigma_{BB}=1.04a_0$. The stiffnesses k are either $k_{AA}=k_{AB}=25\epsilon/a_0^2$, $k_{BB}=100\epsilon/a_0^2$ for hard inclusions, or $k_{BB}=k_{AB}=25\epsilon/a_0^2$, $k_{AA}=100\epsilon/a_0^2$ for soft inclusions. In order to clearly distinguish elastic effects from other possible contributions, we also carried out simulations for an elastically homogeneous system without elastic misfit. In this case, we use $\sigma_{BB}=a_0$ (and the stiffnesses are arbitrary since they do not enter the calculation). In all cases, the temperature is $T=0.5\epsilon/k_B$, which is about half of the critical temperature for phase separation, and the vacancy concentration is taken to be 10^{-3}.

The simulation cell is an hexagon with sides of length $512a_0$. Fixed boundary conditions are applied to the QCM equations at the edges of the simulation cell. For the TDDFT equations, the average occupations at the edges are also fixed, and either open boundary conditions (the edges act as sources or drains of occupation probability) for growth simulation or closed boundary conditions (the edges do not act as sources or drains) for relaxation simulations, are used. A small inclusion composed of B-type atoms is initially placed at the center of the cell; the initial inclusion is a circle with a radius of $10a_0$.

B. Data analysis method

The natural way to study the coarsening behavior of an inclusion is to obtain the so-called Gibbs-Thomson (GT) relation. This relation links the size of the inclusion with either its chemical potential or the solute concentration close to its interface. The coarsening behavior of a collection of inclusions of different sizes can then be inferred from the GT relation since diffusion will occur from regions of high chemical potential (or concentration) toward regions of low chemical potential (or concentration). The system under study here is a ternary mixture (ABv), and two distinct chemical potentials can be defined: μ_A and μ_B. However, the information contained in these two quantities can be summarized in the dimensionless quantity $(\mu_B-\mu_A)/k_BT=\Delta\mu/k_BT$. This can be rationalized as follows. Suppose that the activities in the matrix are given by $\mathcal{A}_m^A$ and $\mathcal{A}_m^B$, while the activities in the inclusion are given by $\mathcal{A}_i^A$ and $\mathcal{A}_i^B$. If the inclusion is in equilibrium with the surrounding matrix, we have $\mathcal{A}_i^A=\mathcal{A}_m^A$ and $\mathcal{A}_i^B=\mathcal{A}_m^B$. If, on the other hand, the matrix is slightly supersaturated, we will have $\mathcal{A}_i^B<\mathcal{A}_m^B$ and, by Eq. (14), there will be an occupation probability flux of B-type atoms of magnitude proportional to $\mathcal{A}_m^B-\mathcal{A}_i^B$ toward the inclusion, i.e., the inclusion will grow. However, since the average occupation within the inclusion is a slowly varying function of the radius, the occupation probability flux of B-type atoms must be compensated by an inverse flux of A-type atoms. In this case, Eq. (14) implies that $\mathcal{A}_m^B-\mathcal{A}_i^B\simeq\mathcal{A}_i^A-\mathcal{A}_m^A$. From this, we can infer that the growth rate of an inclusion is proportional to $(\mathcal{A}_m^B-\mathcal{A}_m^A)-(\mathcal{A}_i^B-\mathcal{A}_i^A)$, i.e., inside a given matrix, the growth rate of an inclusion is solely a function of the difference in activity inside the inclusion. This also means that, if we now consider an ensemble of inclusions inside a given matrix, those in which $\mathcal{A}_i^B-\mathcal{A}_i^A>\mathcal{A}_m^B-\mathcal{A}_m^A$ will shrink to the benefit of those in which $\mathcal{A}_i^B-\mathcal{A}_i^A<\mathcal{A}_m^B-\mathcal{A}_m^A$. Since $\mathcal{A}^\alpha=\exp(\mu^\alpha/k_BT)$, the information about the coarsening behavior of inclusions is also contained in $\Delta\mu$. In what follows, the GT relation of $\Delta\mu$ vs r will thus be used to characterize the equilibrium behavior of inclusions.

C. Homogeneous system without elastic misfit

In order to clearly isolate elastic effects from others, we first present the results obtained with our approach for a system in which no elastic misfit is present. This will serve as a basis for comparison to elastically inhomogeneous systems. We start by discussing the equilibrium properties of the inclusions, then investigate how these are affected by growth at different rates.

1. Equilibrium properties

In the absence of elastic effects, the equilibrium properties of an isolated inclusion are solely a function of the curvature of the interface with the matrix. The prefered shape is a circle at high enough temperature (which is the case here) or a compact faceted shape otherwise; indeed, this is what we observe in our TDDFT simulations.

Since the chemical potential inside an inclusion is a function of interface curvature, $\Delta\mu$ should follow the well-known Gibbs-Thomson relation for circular inclusions:

$$\frac{\Delta\mu(R)}{k_BT}=\frac{C}{R}+\frac{\Delta\mu_\infty}{k_BT}, \tag{16}$$

where R is the radius, C is a constant related to the interfacial free energy, and $\Delta\mu_\infty$ is the value of $\Delta\mu$ inside an infinitely large inclusion. The results are thus best presented as a so-called Gibbs-Thomson plot, where $\Delta\mu$ is plotted against the reciprocal characteristic length of the inclusion. (In the simulation results, the characteristic length is taken to be the radius of a circle with the same area as the inclusion and will be denoted R_{eq}). The normal behavior of $\Delta\mu$ then appears as a straight line. Figure 2 shows the GT relation obtained from a simulation carried out at very low supersaturation ($\Delta c^B=1\%$, where Δc^B is the excess concentration of solute atoms in the matrix relative to the concentration at phase coexistence). The data reproduce the expected $1/R$ dependence of the chemical potentials and thus follows the GT relation.

In Secs. III C 2–4, the dynamical properties of the inclusions are investigated. More specifically, we wish to assess the stability of the circular shape against growth. We also study the effect of growth on the chemical potentials of the inclusions and infer the consequences on the coarsening behavior. To address these questions, different growth rates were imposed to initially circular inclusions. The level of supersaturation of the matrix was varied from directly above the spinodal limit (where new inclusions would spontaneously appear in the matrix) to the binodal limit (where the growth rate vanishes for very large inclusions), thus covering a large portion of physically possible growth rates. At the temperature where the calculations were carried out, the spinodal limit corresponds to a maximal supersaturation Δc^B of about 10%. We begin by exploring the stability of the

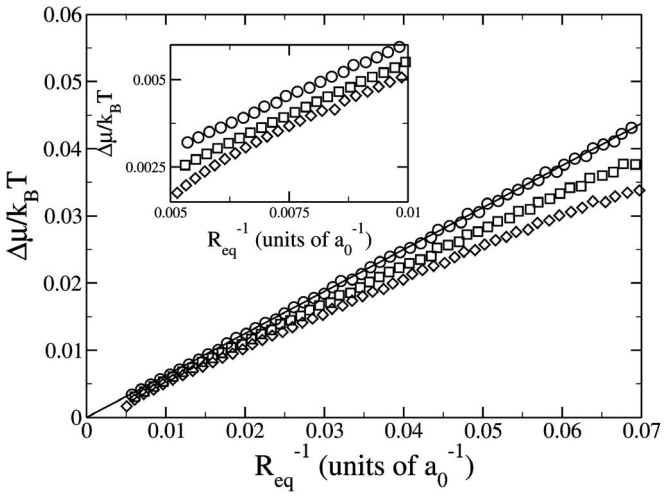

FIG. 2. Dynamical Gibbs-Thomson relations for homogeneous inclusions: circles: $\Delta c^B=1\%$ (quasi-static growth); squares: $\Delta c^B=4\%$; diamonds: $\Delta c^B=10\%$; continuous line: fit to Eq. (16) for $\Delta c^B=1\%$.

equilibrium shape against growth and deformation.

2. Morphological stability

A stroboscopic view of the evolution of the inclusion is provided in Fig. 3 for a very high supersaturation ($\Delta c^B=10\%$). Initially, the inclusion maintains its equilibrium circular shape. As the size increases, the inclusion adopts an increasingly hexagonal shape. Eventually, the "facets" of this hexagon become concave, leading to the formation of pointed tips at the vertices. Near the end of the simulation, the tips split and continue to grow while small bulges appear in their vicinity. The "facets" do not align in directions of low interface energy, so that the anisotropy of the interfacial energy (automatically present because of the underlying symetry of the lattice) is not the primary cause for the sixfold symmetry.

Growth instabilities are well known and commonly observed, both in simulations and in experiments [5–9,38]. The theoretical study of this phenomena was pioneered by Mullins and Sekerka (MS) [5], who developed a model to explain shape instabilities in diffusion-controlled systems by studying the dynamics of infinitesimal perturbations around the equilibrium state. The evolution of these perturbations is governed by two opposing forces, namely, capillarity, which favors the decay of the perturbations, and the so-called point effect of diffusion, which promotes their growth. The point effect is related to the bunching of isoconcentration lines above protuberances on a growing interface and to their rarefaction above depressions. The net result is the focusing of diffusion fluxes away from the depressions and toward the protuberances, thus increasing the amplitude of the perturbation.

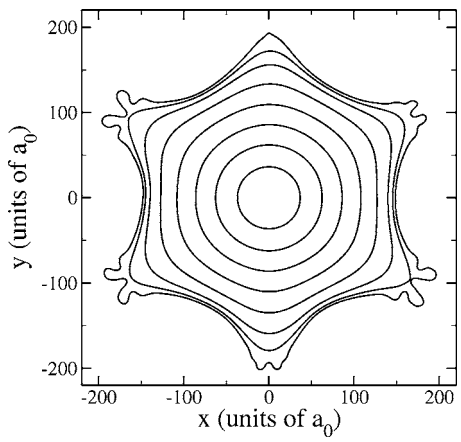

FIG. 3. Evolution of a growing homogeneous inclusion for $\Delta c^B=10\%$ over $1.5\times10^{12}\tau_0$.

In the case of a perturbed circular inclusion, the distance between the center of the inclusion and a given point on its interface with the matrix can be decomposed into a sum of contributions from different modes, i.e., $r(\theta)=R+\Sigma_l\delta_l\cos(l\theta+\phi_l)$, with δ_l the amplitude of mode l and ϕ_l its associated phase. MS showed that the fractional rate of increase (FRI) of the amplitude of a mode is given by:

$$\frac{\dot{\delta}_l/\delta_l}{\dot{R}/R}=(l-1)\left[1-\frac{R_c(l)}{R}\right]\left[1-\frac{R^*}{R}\right]^{-1}, \tag{17}$$

with R^* the thermodynamical critical radius of an inclusion at the imposed supersaturation and $R_c(l)=[(1/2)(l+1)(l+2)+1]R^*$ the critical radius for the amplification of mode l. [Below $R_c(l)$ mode l decays, whereas above $R_c(l)$ it grows.] The sign of the FRI indicates whether a perturbation of the corresponding mode grows (+) or decreases (–). Furthermore, a FRI between 0 and 1 indicates that, while the amplitude of the mode grows, it does so less rapidly than the radius of the inclusion, so that the equilibrium shape will be asymptotically restored. In constast, a FRI higher than 1 indicates that the relative contribution of the mode to the overall shape increases with time.

Two important conclusions can be inferred from Eq. (17). First, the radius at which a mode becomes unstable increases rapidly with its order. This means that only low-order modes are expected to be relevant for the range of sizes probed here. Second, the higher the order of a mode, the higher its asymptotic FRI is [the FRI tends to $l-1$ for $R\gg R_c(l)$].

It is useful to recall that the MS theory is linear in that it assumes vanishingly small perturbation amplitudes, so that interactions between modes can be neglected. Thus, in order to compare the simulation results to the theory, we need to study configurations where only one mode is significantly excited. To achieve this, simulations were initialized with inclusions whose shape is perturbed by either mode 2 or mode 3 [$\delta_2(t=0)=1$ or $\delta_3(t=0)=1$]. Note that, even in this case, nonlinear effects cannot be excluded because other modes will progressively get excited during the evolution of the system. We will return to the case of the initially unperturbed inclusion below.

The FRI inferred from these simulations are reported in Fig. 4 for different levels of supersaturation. The agreement between the data and the predictions of the model is reasonable. The initial increase of the FRIs close to R_c and their asymptotic value are well reproduced.

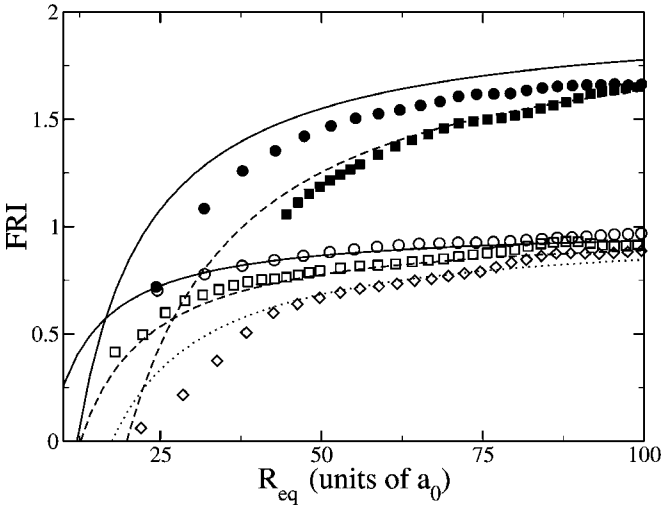

FIG. 4. Fractional rate of increase of modes 2 and 3 for perturbed homogeneous inclusions: circles: $\Delta c^B=10\%$; squares: $\Delta c^B=7\%$; diamonds: $\Delta c^B=3\%$; continuous lines: Eq. (17) with $R^*=1.1a_0$ for $l=2$ and $l=3$; dashed lines: Eq. (17) with $R^*=1.8a_0$ for $l=2$ and $l=3$; dotted line: Eq. (17) with $R^*=2.5a_0$ for $l=2$. The empty symbols correspond to $l=2$ and the filled ones to $l=3$.

However, discrepancy with the theory appears as perturbations develop further. As mentioned earlier, this is due to interactions between modes. The most important consequence is the excitation of higher-order harmonics of strongly excited modes. This can be observed in Fig. 5, where the FRIs of a few modes for a simulation with a strong initial perturbation of mode 3 $[\delta_3(t=0)=2a_0]$ are reported. The results show that the FRI of mode 6 reaches more than twice the expected value because of interactions with mode 3. We have carried out a series of simulations to confirm that this excess FRI is indeed directly correlated with $\delta_3(t=0)$. The FRIs of mode 3 and 6 then gradually decrease. Both the

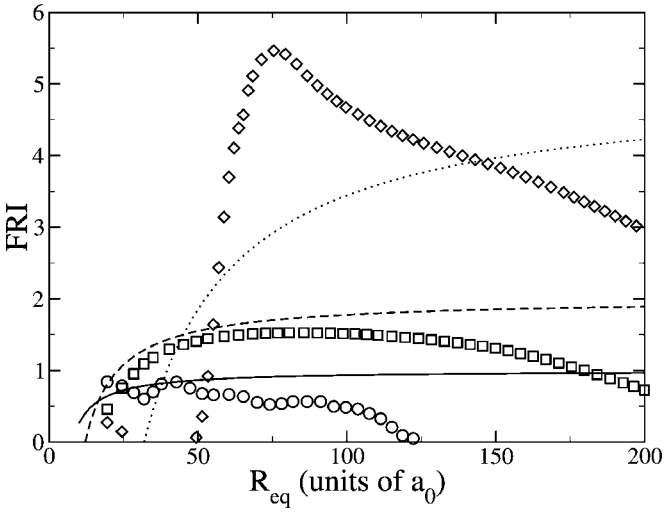

FIG. 5. Fractional rate of increase for homogeneous inclusions with $\delta_3(t=0)=2a_0$ for $\Delta c^B=10\%$: circles: mode 2; Squares: mode 3; diamonds: mode 6; continuous line: Eq. (17) with $R^*=1.1a_0$ for $l=2$; dashed line: Eq. (17) with $R^*=1.1a_0$ for $l=3$; dotted line: Eq. (17) with $R^*=1.1a_0$ for $l=6$.

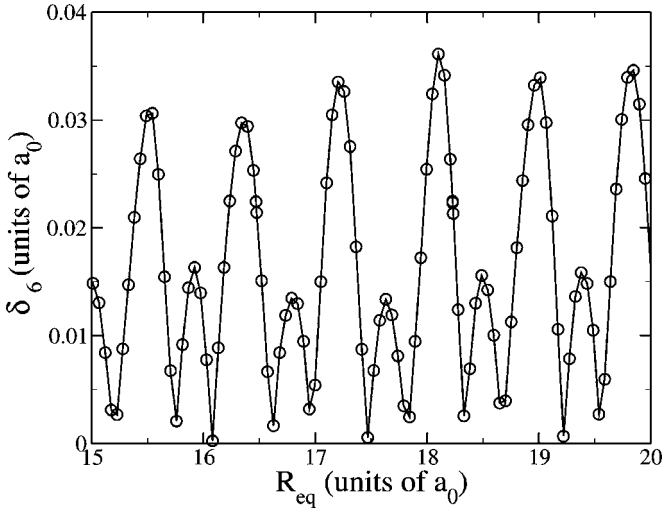

FIG. 6. Amplitude of mode 6 for a homogeneous inclusion at $\Delta c^B=0.1\%$.

excitation of higher-order harmonics and the inhibition of large-amplitude modes are known consequences of nonlinearities [7]. The other commonly observed effect is the inhibition of incommensurate modes. This effect can also be observed in Fig. 5. In this case, the growth of mode 2 is strongly inhibited by the large amplitude of mode 3. This process is so efficient that mode 2 actually becomes stable around $R=125a_0$ (when the FRI becomes negative).

3. Excitation of perturbations

Up to now, we have focused on the amplification of perturbations. Of course, they need to be created before they can be amplified. In real systems, the MS instability feeds on random thermal fluctuations while in deterministic and isotropic numerical models, the only source of instability is numerical noise (roundoff or integration errors, for example). In the present case, the microscopic resolution causes the isotropy to be broken. Indeed, the inclusion grows on a discrete lattice with sixfold rotational symmetry. This causes angular variations of various physical quantities which can couple with the inclusion shape and induce shape modulations. This phenomenon can be observed in Fig. 6, where the amplitude of mode 6 for an initially circular inclusion at very low supersaturation is reported. Below $R_c(6)$, the amplitude of this mode indeed exhibits an oscillatory behavior of period a_0. Note that in the range of radii of Fig. 6, the amplitudes of the other modes are 1 or 2 orders of magnitude below that of mode 6. Furthermore, the phase of mode 6 relative to the underlying lattice is constant from one simulation to another, which supports the idea of an excitation through interactions with the lattice. Other modes can then be excited either by direct coupling with mode 6 or by interaction of the slightly perturbed shape with the lattice, in addition to numerical noise. This demonstrates the power of our approach for studying phenomena that emerge from the existence of fundamental symmetries or length scales.

The above discussion enables us to understand the evolution of initially unperturbed shapes, such as that shown in

Fig. 3. If we assume that the primary mode-excitation process is noise, the MS theory predicts that different shapes should be observed as a function of the supersaturation: low-index modes should tend to dominate at low supersaturations, while high-index modes prevail at higher supersaturation. However, this is not what we observe: mode 6 invariably emerges as the leading mode when the radius of the inclusion exceeds $R_c(6)$. Even as the supersaturation increases, higher-index modes with asymptotically larger FRIs are not able to outgrow mode 6 in the range of sizes probed here. This shows that the preferential excitation of mode 6 by the lattice is the cause of its dominance in the shape of initially circular inclusions. We also observe that the excitation of other modes is extremely sensitive to noise: indeed, their relative contribution to the shape of the inclusion varies from one simulation to the other even for identical initial conditions (modulo the inevitable numerical roundoff errors).

Another factor related to the anisotropy of the lattice contributes to the observed dominance of mode 6: the anisotropy of the mass transport and interface kinetics. Indeed, anisotropic kinetics are known to induce faceting [9] and the formation of corners [7,8] and tips; it is also known to delay the well-known tip splitting instability, as clearly shown by Brush and Sekerka [7]. These results indicate that in completely isotropic systems, even very blunt tips split spontaneously, while the introduction of kinetic anisotropy gradually stabilizes them. By comparing Fig. 3 to the morphologies reported in Ref. [7], it is clear that such mechanisms operate in our simulations. However, the quantitative agreement between the measured FRIs and the predictions of the isotropic MS model indicates that, at least below $R=100a_0$ (where nonlinear effects are small), the anisotropy of the kinetic coefficients is not the dominant factor in the growth of the different modes.

These results highlight another advantage of our approach compared to MMS: the anisotropy of the kinetics and of the energetics is automatically taken into account because of the microscopic formulation of our model. This makes the task of identifying and parametrizing these anisotropies *a priori* unnecessary.

4. Dynamical corrections to the GT relation

Having analyzed the role of dynamical effects on the topology of the inclusions, we now turn to a discussion of their impact on the chemical potential and, hence, on their coarsening behavior. Figure 2 shows that finite growth rates can have a significant effect on the GT relation of the inclusions. Although the general behavior is preserved, the slope of the GT curve shows a clear rate dependence. This, in turn, implies that the composition of the inclusion is a function of the growth rate. This dependence is a consequence of the so-called solute trapping effect, which is also observed in such contexts as rapid solidification in alloys [39,40] and grain coarsening in polycrystalline materials [41], for example (see Ref. [42] for a recent review). The solute trapping effect can be understood intuitively using a simple argument [40]: under growth conditions, a concentration gradient forms in front of the growing interface; since there is a free energy cost associated with this concentration gradient, the equilibrium partition of solute atoms across the interface can be ignored in favor of smaller gradients. By using this assumption to solve the diffusion equation for a system with an interface traveling at constant velocity, Langer and Sekerka [43] showed that the solute concentration in the growing phase should vary linearly with the interface velocity.

The topology of the inclusions also affects the GT relation through a slight downward curvature at large size (see inset to Fig. 2). Clearly, this contribution could become quite significant at larger sizes and for more pronounced shape perturbations, but for the range of sizes studied here, it is very small.

Although the absolute value of the dynamically induced chemical potential shift (as measured by the distance between the quasistatic GT curve and the dynamical one) may seem important, it has to be compared to the driving force necessary to induce such a shift, i.e., for the shift to be really significant, it has to be comparable to the driving force ($\Delta\mu/k_BT$ at the boundary of the simulation cell minus $\Delta\mu/k_BT$ in the inclusion) or else its impact on growth dynamics will be negligible. For $\Delta c^B=10\%$, the driving force is ~ 0.7 while the shifts are of the order of 0.01 or smaller. Even for $\Delta c^B=4\%$ the driving force is still large (~ 0.6). Thus, the dynamically induced shifts are too small to significantly affect the coarsening behavior of the inclusions. For this reason, we will not try to quantify precisely the solute trapping process nor the impact of the shape perturbation on the chemical potentials in the present study.

D. Hard inclusions

1. Equilibrium properties

Having studied the reference homogeneous system, we now turn to the case of hard inclusions. For isotropic elasticity, Eshelby [44] showed that a circular inclusion has a lower elastic energy than an ellipse. Because, at high enough temperature, the interface-energy minimizing shape is also a circle, hard inclusions have a circular shape independent of their size. In quasistatic growth simulations, we also observe quasicircular shapes for all sizes investigated ($10a_0<R<100a_0$). However, we observe a slight departure from the circular shape through the formation of "facets." These are not facets in the strict thermodynamical sense, but shape modulations resulting from a tendency of the interface to align with atomic planes which have low interface energies. Note that this phenomena is not present in homogeneous inclusions, where the amplitude of mode 6 oscillates but does not to grow until $R_c(6)$ is exceeded (c.f. Fig. 6). This behavior can be explained by a strain-induced change of the orientational dependence of the interfacial free energy. This effect, and its dynamical consequences, will be described elsewhere. The small magnitude of this (nearly rate-independent) shape variation can be appreciated from Fig. 7: the amplitude of mode 6 remains below 0.5% of the radius of the inclusion in the range studied. Also, the amplitude of mode 6 is not a linear function of the radius, i.e., large inclusions are not scaled-up versions of small ones. This may be a consequence of the interface contributions to the elastic energy which are not negligible for inclusions below a few

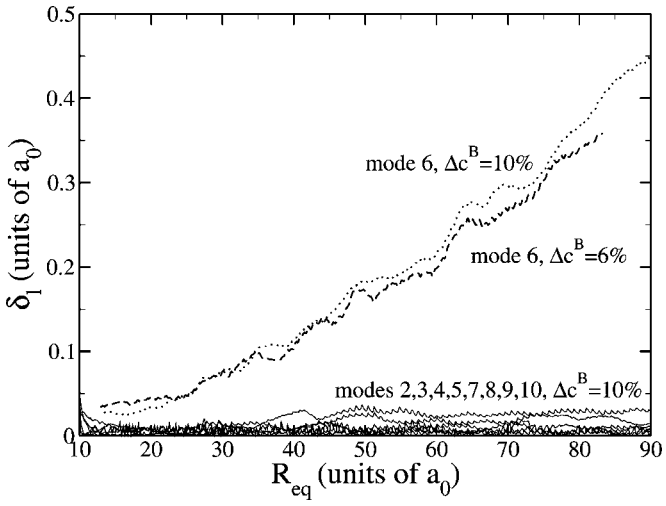

FIG. 7. Amplitude of various perturbation modes as a function of size for hard growing inclusions: dotted line: mode 6 for $\Delta c^B=10\%$; dashed line: mode 6 for $\Delta c^B=6\%$; thin continuous lines: modes 2–10 excluding 6 for $\Delta c^B=10\%$.

tens of nanometers [45]. This highlights another strength of our model: because of its microscopic formulation, scale-dependent effects are automatically taken into account.

In the continuum limit, the strain inside a circular inclusion is independent of its size [33]. Thus, the normal Gibbs-Thomson behavior should be observed for hard inclusions (modulo the small contributions from facet formation). This is indeed the case, as shown in Fig. 8 for $\Delta c^B=1\%$ (smaller supersaturations give similar results). The effect of the elasticity is thus to modify the values of C and $\Delta\mu_\infty$, in agreement with the sharp-interface results of Thornton and collaborators [46]. In addition, the figure shows rather strong oscillations in the chemical potential, with a period of $0.866a_0$. These oscillations are related to variations in the energy required to incorporate an additional atom along the

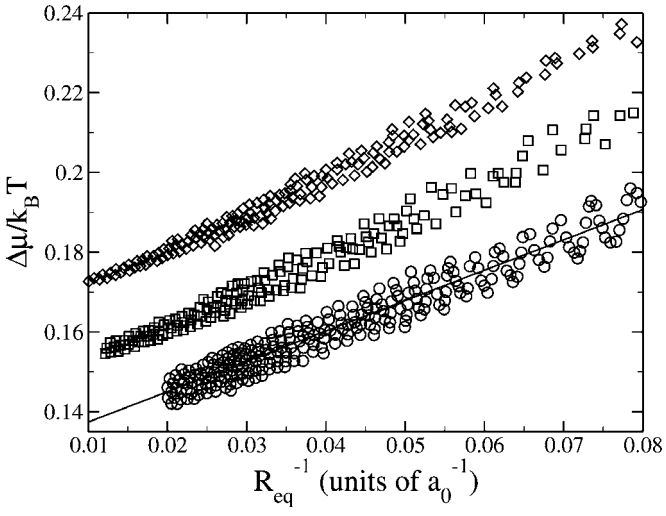

FIG. 8. Dynamical Gibbs-Thomson relations for hard inclusions: circles: $\Delta c^B=1\%$ (quasistatic growth); squares: $\Delta c^B=4\%$; diamonds: $\Delta c^B=10\%$; continuous line: fit to Eq. (16) for $\Delta c^B=1\%$.

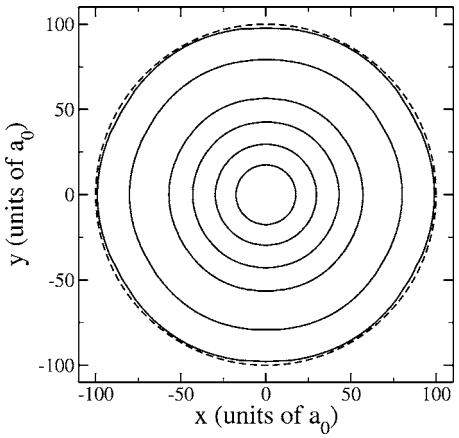

FIG. 9. Evolution of a growing hard inclusion for $\Delta c^B=10\%$ over $1\times10^{12}\tau_0$. The dashed line represents a perfectly circular inclusion with $R_{\mathrm{eq}}=100a_0$.

interface. Indeed, because the inclusion's shape is not perfectly isotropic, the elastic energy cost for the addition of a B atom varies as a function of position along the interface. During growth, the available sites will be filled in order of increasing energy; since the chemical potential corresponds to the free energy change on adding a B atom at the interface, it will gradually increase until new low-energy sites become available, and the cycle repeats itself. A detailed analysis of this phenomenon, and its importance for coarsening, will be reported elsewhere [47].

2. Morphological stability

As expected, elasticity does not induce qualitative changes in the equilibrium properties of hard inclusions compared to homogeneous inclusions. However, dynamical properties may be affected by elasticity. To clarify these matters, simulations of growth were here again carried out.

Figure 9 shows the evolution of the shape of a hard inclusion during growth. Compared to the homogeneous inclusion, the (quasi)circular hard inclusion appears to be very stable: the formation of concave interfaces or tips is inhibited even at very large supersaturation. The facets mentioned earlier become more evident when comparing to a perfectly circular inclusion (dashed line). The small depressions appear when the orientation of the interface is nearly parallel to a low-interface energy direction (occuring at odd multiples of $\pi/6$ in the present calculations). We may quantify these morphological changes using a modal decomposition; the results are reported in Fig. 7.

We find that a perturbation along mode number 6 indeed develops as the size of the inclusion increases. The data also indicates that modes other than 6 are completely frozen for the range of sizes examined here: small variations can be observed, but no amplification occurs. Since not even the low-index modes are allowed to grow (indicating high critical radii), it would be rather surprising that mode 6 could be dynamically amplified. In fact, our simulations show that the amplitude of mode 6 does not depend on supersaturation in the range of supersurations probed here (see Fig. 7). Hence, the growth of this mode is probably, rather, a manifestation

of a change in the equilibrium shape of the inclusion, as mentioned above. These results indicate that elasticity leads to a very effective stabilization of circular inclusions in the size domain investigated.

This stabilization of the inclusion against perturbations was predicted by Leo and Sekerka [6] who extended the model of Mullins and Sekerka [5] to include the effects of elasticity. Qualitatively, they found that elasticity stabilizes hard inclusions by decreasing the growth rate of perturbations, by increasing the critical radius for mode amplification, and by decreasing the wavelength of the fastest growing perturbation. Quantitatively, this can be taken into account by modifying the FRI of the amplitude of perturbations compared to the elastically homogeneous case, which becomes [c.f. Eq. (17)]

$$\frac{\frac{\dot{\delta}_l}{\delta_l}}{\frac{\dot{R}}{R}} = (l-1)\left[1-\frac{l+1}{l-1}\frac{g^{\mathrm{el}}(l)}{2\gamma}R^*\right]\left[1-\frac{R_c l}{R}\right]\left[1-\frac{R^*}{R}\right]^{-1}, \tag{18}$$

where the critical radius for mode amplification is given by

$$R_c(l) = \frac{\left[\frac{1}{2}(l+2)(l+1)+1\right]R^*}{1-\frac{l+1}{l-1}\frac{g^{\mathrm{el}}(l)}{2\gamma}R^*}, \tag{19}$$

with $g^{\mathrm{el}}(l)$ a factor related to the elastic properties of the material [$g^{\mathrm{el}}(l)=0$ for homogeneous systems] and γ is the interface energy per unit length. From Eqs. (18) and (19), one can see that a positive value of $g^{\mathrm{el}}(l)$ (corresponding to hard inclusions) results in a decrease of the asymptotic FRI of every mode and an increase of the critical radius for mode amplification, $R_c(l)$, in agreement with our observations. In order to verify if our model quantitatively reproduces the predictions of Leo and Sekerka [6], we studied the decay of initially imposed perturbations similar to the case of homogeneous inclusions. Since the decay of perturbations is very fast for small sizes (except for low-index modes and high supersaturations), only the FRI of mode 2 at high supersaturation could be computed reliably. The results are presented in Fig. 10. By comparing to Fig. 4, one clearly observes the strong decrease of the FRI induced by elasticity, with an asymptotic value close to 0 already at a supersaturation of 7%. A reasonable fit to the data can be obtained using $g^{\mathrm{el}}(l)/2\gamma=0.16$ and the values of R^* from homogeneous inclusions. Although qualitative agreement can be claimed, it is difficult to give a quantitative assessment based only on the limited data available. Nevertheless, the general conclusions of Leo and Sekerka [6] concerning the effect of elasticity are certainly verified.

3. Dynamical corrections to the GT relation

Even if dynamical effects do not induce shape changes in hard inclusions under the conditions studied here, the GT relations turn out to be strongly affected by growth, as can be appreciated from Fig. 8 where the GT curve is plotted for different levels of supersaturation. The results show that the normal GT behavior is observed during rapid growth. However, large shifts in the chemical potential as a function of supersaturation are measured. These are once again caused by solute trapping. The large value of these shifts compared to the homogeneous case is related to the strong coupling between strain and occupation probability fields, i.e., changes in the occupation probabilities induces changes in the strain field, which, in turn, affect the chemical potentials, causing further changes in the occupation probabilities, etc. Although the shifts are larger here than in the homogeneous case, they are still small compared to the driving force (0.04 vs ~0.9 at $\Delta c^B=10\%$ and 0.02 vs ~0.64 at $\Delta c^B=4\%$), so, once again, the dynamical corrections are not expected to significantly affect the coarsening behavior of hard inclusions.

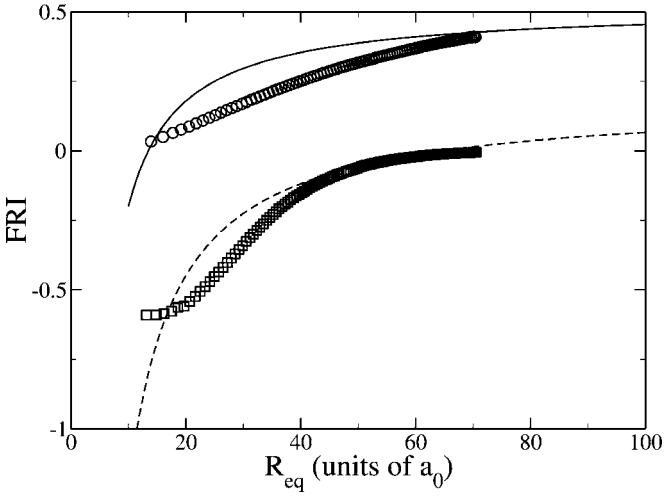

FIG. 10. Fractional rate of increase of mode 2 for hard inclusions: circles: $\Delta c^B=10\%$; squares: $\Delta c^B=7\%$; continuous line: Eq. (18) with $g^{\mathrm{el}}(l)/2\gamma=0.16$ and $R^*=1.1a_0$; dashed line: Eq. (18) with $g^{\mathrm{el}}(l)/2\gamma=0.16$ and $R^*=1.8a_0$.

E. Soft inclusions

The case of soft inclusions is much more complex. Indeed, it is known since Eshelby [44] that a soft circular inclusion possesses higher elastic energy than an elliptical one. However, the interfacial component of the free energy favors the more compact circular shape. Thus, one would expect a transition from an interface-dominated regime with circular inclusions (at small sizes) to an elastic-dominated regime with ellipsoidal inclusions (at large sizes). This transition was studied using very general symmetry considerations by Johnson and Cahn [2] who showed that, in two dimensions, a second-order transition in the aspect ratio of inclusions occurs as their size increases. In the following, the consequences of this shape transition on the equilibrium and dynamical properties of the inclusions will be explored.

1. Equilibrium properties

For reasons that will become clear below, growth simulations cannot be used to probe the equilibrium properties of

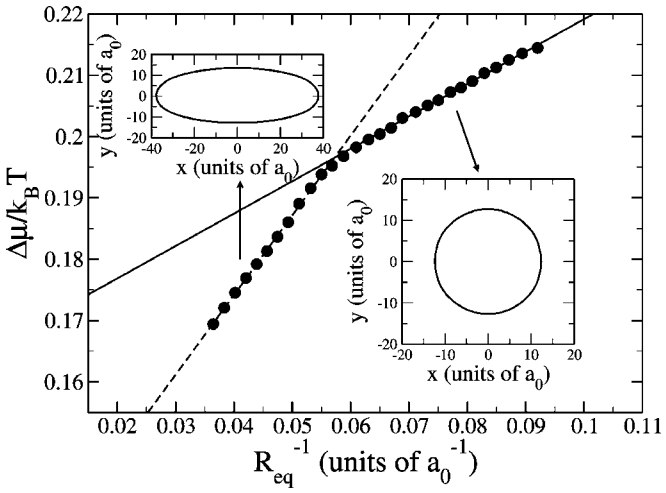

FIG. 11. Equilibrium Gibbs-Thomson relation for soft inclusions. Left inset: equilibrium shape of the inclusion for $R_{eq}=23a_0$; right inset: equilibrium shape of the inclusion for $r_{eq}=13a_0$.

soft inclusions. Instead, a sequence of relaxations for inclusions of different sizes with closed boundary conditions was performed. Using this method, the expected shape transition was indeed observed, as can be seen in the insets of Fig. 11. As predicted, there is a maximum size over which circular inclusions are not stable: they adopt instead increasingly eccentric elliptical shapes. Furthermore, the onset of this shape transition is very abrupt, in agreement with the predictions of Johnson and Cahn [2].

Figure 11 also provides, through a GT plot, a quantitative view of the effect of the transition on the thermodynamic properties of the inclusions. First, the transition is clearly marked by a discontinuity in the slope at $R^{-1}=0.59a_0^{-1}$ ($R \simeq 17a_0$). Second, the change in slope is very significant—a factor of about 2.5. This is consistent with the results of Li *et al.* [4], where the effect of the shape transition induced by anisotropic and inhomogeneous elasticity was studied. However, the magnitude of the change observed here is larger than reported in their study, probably due to the larger elastic inhomogeneity used here. The consequences of this change

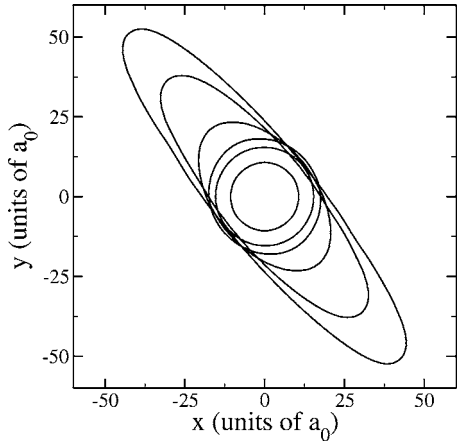

FIG. 12. Evolution of a growing soft inclusion for $\Delta c^B=0.1\%$ over $5\times10^{12}\tau_0$.

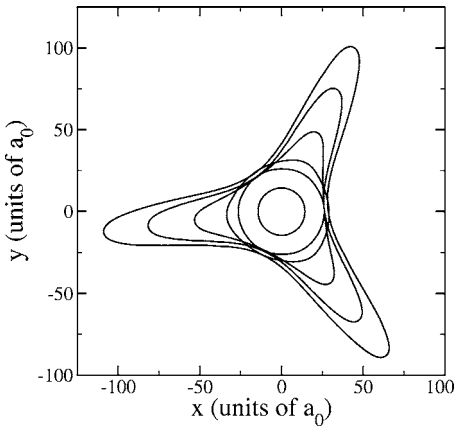

FIG. 13. Evolution of a growing soft inclusion for $\Delta c^B=0.5\%$ over $3\times10^{12}\tau_0$.

of slope on the coarsening behavior of a collection of soft inclusions will be discussed in Sec. IV.

2. Morphological stability

The presence of a shape transition during growth opens up the possibility of a complex behavior because metastable states, where both composition and shape are out of equilibrium, are now accessible. Since shape relaxation can be quite slow, the behavior of the inclusions is likely to be affected by dynamical effects over long periods of time. To test this hypothesis, simulations for various growth rates were carried out.

On the basis of mere visual inspection, it is already clear that elasticity has a dramatic impact on the shape adopted by the inclusions during growth. Examples of such shapes are presented in Figs. 12–14 for different values of the supersaturation. First, at very low supersaturation (0.1%), Fig. 12 shows that the equilibrium shape is preserved during growth: circles at small sizes, ellipses at larger sizes. In the latter regime, the major axis grows much more rapidly than the minor axis, leading to increasingly eccentric shapes. Second, for a slightly higher, but still very low supersaturation by homogeneous or hard inclusion standards (0.5%), the evolu-

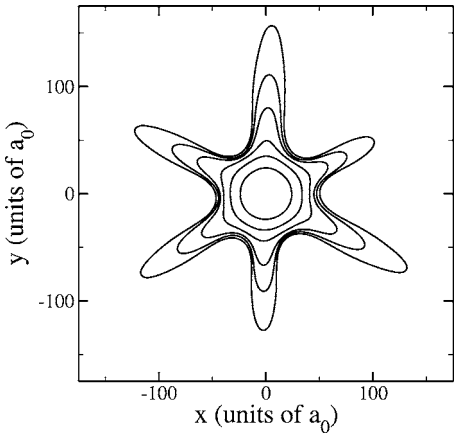

FIG. 14. Evolution of a growing soft inclusion for $\Delta c^B=10\%$ over $7\times10^{11}\tau_0$.

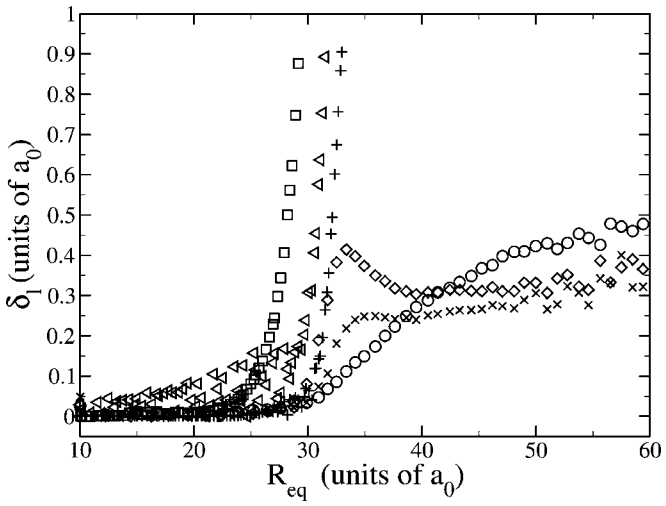

FIG. 15. Amplitude of various perturbation modes as a function of inclusion size for a soft growing inclusions with $\Delta c^B=0.5\%$: circles: mode 2; squares: mode 3; diamonds: mode 4; triangles: mode 6; ×: mode 7; crosses: mode 9.

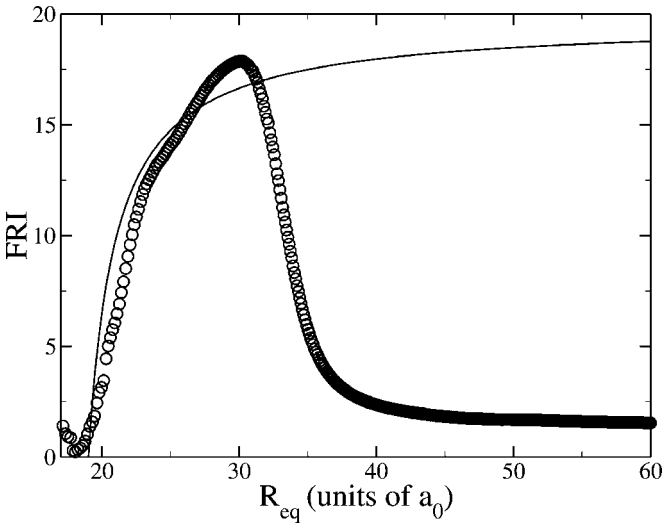

FIG. 16. Fractional rate of increase of mode 3 for the soft inclusions depicted in Fig. 13 ($\Delta c^B=0.5\%$): circles: simulation results; continuous line Eq. (18) with $g^{el}(l)/2\gamma=-0.26$ and $R^*=17a_0$.

tion of the system is completely different. Instead of a shape transition from circle to ellipse, a transition toward a threefold symmetric shape is observed, as shown in Fig. 13. Here, growth proceeds essentially from the tips of the inclusion. The important point is that this nonequilibrium shape is stable in time, i.e., it does not decay toward an ellipse as long as the flux is maintained. Surprisingly, only a very small supersaturation is required to achieve this. Third, for high supersaturations, Fig. 14 shows that sixfold symmetry is preferred. Once again, this shape is stable in time and growth occurs almost exclusively from the tips. It is interesting to note that we did not observe any tip-splitting instability in soft inclusions, unlike in the case of homogeneous inclusions, even at very high growth rates. Finally, for intermediate supersaturations, we also observed shapes with four or five tips. Note that, although there is a clear correlation between supersaturation and morphology, the relation between the two is not absolute: we observed that more than one type of inclusion may form from the same initial conditions.

The formation of shapes of increasingly higher order as supersaturation increases can be understood using the Mullins-Sekerka theory. Indeed, it predicts that the order of the fastest growing mode is proportional to $R^{*-1/2}$ and, hence, to the supersaturation. Thus, as the supersaturation increases, the leading mode, and therefore, the shape of the inclusion, should be of increasingly higher order. For homogeneous inclusions, this tendency is overwhelmed by the preferential excitation of mode 6. For soft inclusions, it seems that other modes are able to overcome this disadvantage. An explanation for this will be offered later on in this section.

A quantitative appreciation of the development of the shape can be obtained from a modal analysis. This is reported in Fig. 15 for the system shown in Fig. 13. The first mode to be amplified significantly is mode 3; note the very high rate at which it develops. Very soon after, two of its harmonics (6 and 9) are also strongly amplified through interactions with the leading mode. Concomitantly, we observe that the growth of other modes is either slowed down or reversed.

A closer look at the FRIs indicates that three regimes are in fact present. This is illustrated in Fig. 16 for mode 3 (similar results are obtained for other modes). The FRI initially increases rapidly to reach extremely high values—the asymptotic FRI for mode 3 is 2 in homogeneous systems [c.f. Eq. (17)]. This increase is followed by a very rapid decrease, after which the FRI finally settles at a low value of ~1.5. The extremely high values of the FRI observed in the early stages of the simulation explain the sensitivity of the results to noise that was noted above: the least perturbation is exponentially amplified so that the balance between the different modes can easily be disrupted. These results also suggest that the rapid change of the FRI observed around $R=30$ marks a change in perturbation growth mode. This possibility will be explored in Sec. III E 3.

When the amplitudes of the perturbations are sufficiently small that nonlinearities can be neglected, the behavior of the shape instability should be correctly described by the Leo-Sekerka generalization of the Mullins-Sekerka theory. In the case of soft inclusions, Eqs. (18) and (19) are still valid, but the predicted value of g^{el} is now negative. The effect of elasticity is therefore to increase the asymptotic FRIs and to decrease the critical radii compared to the homogeneous case, thus strongly favoring shape instabilities. Furthermore, the asymptotic FRI is now proportional to R^*, so that very large values are possible even at small supersaturations. This explains why the relative importance of the preferential excitation of mode 6 is now reduced: very small excitations of other modes can now be amplified very efficiently even before $R_c(6)$ is reached. In order to verify if the Leo-Sekerka theory adequately describes the shape evolution of the inclusions, growth simulations were carried out for inclusions initially perturbed by either mode 2 or 3. The FRI inferred from these simulations are reported in Figs. 17 and 18.

First, the expected increase of the FRI for mode 2 can clearly be seen in Fig. 17 [the asymptotic $R_{eq}\to\infty$ value of

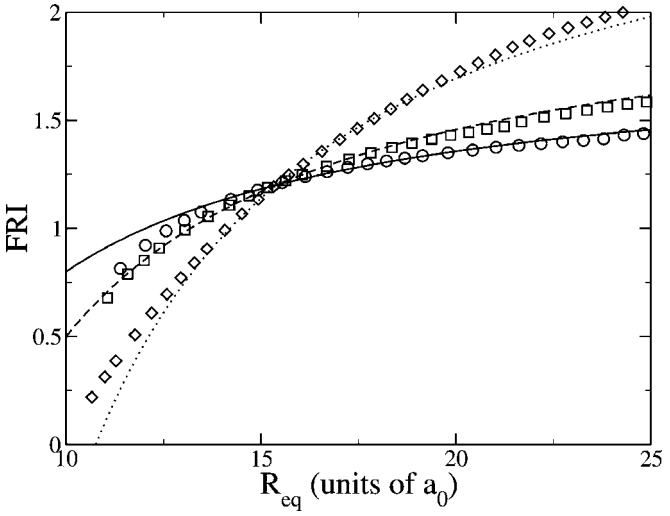

FIG. 17. Fractional rate of increase of mode 2 for soft inclusions: circles: $\Delta c^B=9\%$; squares: $\Delta c^B=6\%$; diamonds: $\Delta c^B=3\%$; continuous line: Eq. (18) with $g^{\mathrm{el}}(l)/2\gamma=-0.13$ and $R^*=1.6a_0$; dashed line: Eq. (18) with $g^{\mathrm{el}}(l)/2\gamma=-0.13$ and $R^*=2.5a_0$; dotted line: Eq. (18) with $g^{\mathrm{el}}(l)/2\gamma=-0.13$ and $R^*=4.5a_0$. All lines are shifted upward by 0.2.

the FRI in the homogeneous case is unity for this mode, c.f. Eq. (17)]. Second, our results are in excellent agreement with the Leo-Sekerka model for $g^{\mathrm{el}}(2)/2\gamma=-0.13$ and appropriate values of R^*. The value of $g^{\mathrm{el}}(l)/2\gamma$ can be very precisely determined here because it fixes the radius at which the FRI for different values of R^* cross. Note that in order to get agreement with the simulations results, the theoretical FRI curves had to be shifted upward by 0.2 (see below).

A similar analysis was performed for mode 3 and the results are reported in Fig. 18. Once again, large enhancements of the FRI (already a factor of two at small sizes and

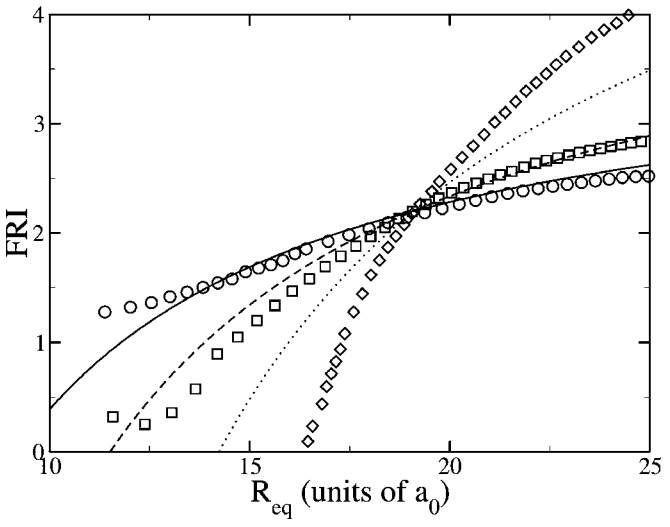

FIG. 18. Fractional rate of increase of mode 3 for soft inclusions: circles: $\Delta c^B=9\%$; squares: $\Delta c^B=6\%$; diamonds: $\Delta c^B=3\%$; continuous line: Eq. (18) with $g^{\mathrm{el}}(l)/2\gamma=-0.26$ and $R^*=1.6a_0$; dashed line: Eq. (18) with $g^{\mathrm{el}}(l)/2\gamma=-0.26$ and $R^*=2.5a_0$; dotted line: Eq. (18) with $g^{\mathrm{el}}(l)/2\gamma=-0.26$ and $R^*=4.5a_0$. All lines are shifted upward by 0.2.

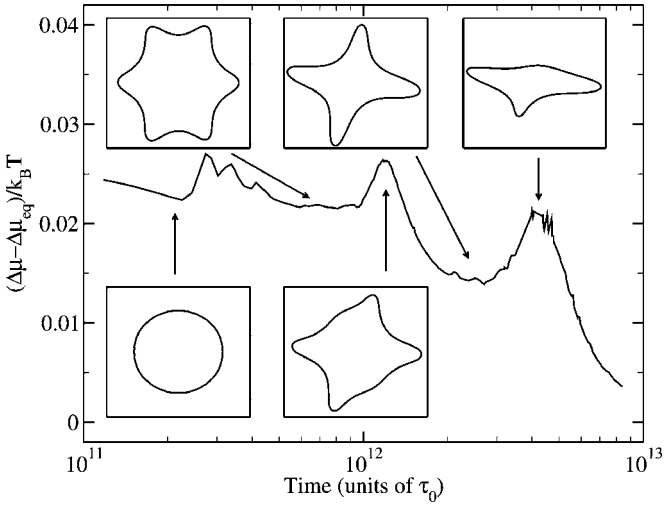

FIG. 19. Relaxation of a circular soft inclusion with $R_{\mathrm{eq}}=40a_0$. Insets: shape of the inclusion at different moments during the relaxation process.

moderate supersaturation) are observed. Good agreement between simulation results and theoretical predictions is achieved with $g^{\mathrm{el}}(3)/2\gamma=-0.26$ and the values of R^* obtained from mode 2, and by shifting the theoretical curves upward by 0.2. Thus, as in the hard inclusion case, the Leo-Sekerka description of growth instabilities provides an adequate account of the simulation results for small inclusions.

The shift of the theoretical FRI curve, necessary to match the simulation data, indicates that another factor besides the Mullins-Sekerka instability contributes to the growth of shape perturbations. One possibility is that the quasistatic relaxation from a circular inclusion larger than the critical size to an elliptic inclusion involves the growth of sinusoidal perturbations, similar to those occurring via the Mullins-Sekerka mechanism, hence, adding a static contribution to the FRI. In order to investigate this hypothesis, we studied the relaxation of a circular inclusion with $R=40a_0$ (for which the equilibrium shape is an ellipse) with closed boundary conditions, i.e., without any diffusion fluxes in or out of the cell. The evolution of the shape of the inclusion and of its distance to equilibrium (as measured by the difference between its chemical potentials and those of an equilibrium inclusion of the same size) is reported in Fig. 19. This figure shows that the relaxation of a circular inclusion towards its equilibrium shape indeed occurs by a succession of transitions, from high- to low-symmetry structures, and not by a continuous and smooth deformation of the circle to an ellipse. This can be seen both in the insets, where the inclusion shape is reported, and in the main graph, where the evolution of $\Delta\mu$ is presented. Simulations show that the order of the dominant quasistatic shape perturbation increases with size, from 2 close to the equilibrium transition point to 12 for large inclusions. The quasistatic relaxation pathway thus provides an explanation for the unexpectedly large FRI and acts so as to further promote the formation of high-order symmetric shapes. Note that very similar relaxation patterns have been observed using conventional microscopic methods [18,19]. This further shows that our model adequatly retains

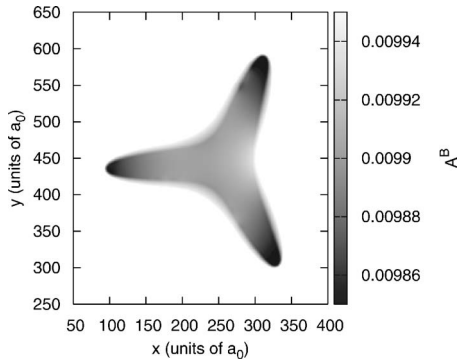

FIG. 20. Activity map of B atoms for a soft inclusion for $\Delta c^B=0.5\%$.

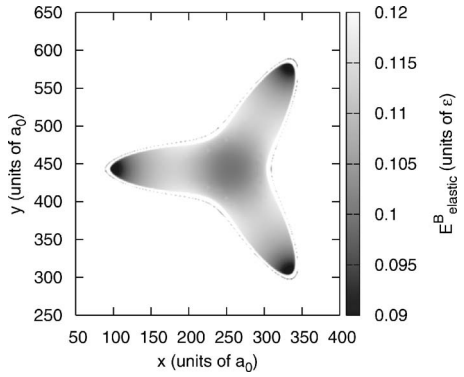

FIG. 21. Elastic energy map of B atoms for a pure-B soft inclusion.

the essential physics from the discrete formulation.

3. Late stages of perturbation growth

The above discussion suggests that the evolution of the shape of the inclusions should, for the most part, be governed by the Mullins-Sekerka instability. Comparing the predictions of the model to the evolution of mode 3 presented in Fig. 16, we see that good agreement is achieved here only for inclusions smaller than $R=30a_0$. For larger sizes, the FRI sharply decreases in contradiction with the behavior predicted by this model. A possible explanation is that the Mullins-Sekerka theory breaks down because of nonlinear interactions between modes similar to that observed in Fig. 5. However, the amplitude of mode 3 is roughly 3% of the radius of the inclusion at $R=30a_0$, compared to 10 to 15% in the homogeneous case, so that, while nonlinear effect are probably affecting the results, it is unlikely that they could induce change in behavior of such large extent.

The nature of the new regime can be inferred from Fig. 13, which shows that growth occurs exclusively at the tips in the later stage of evolution, while the regions close to the core are frozen. The signature of this regime can indeed be identified by examining the activity maps of the system during growth, an example of which is presented in Fig. 20 for B atoms. The data show that the activity is relatively uniform inside the inclusion, except at the end of the tips where minima form. Since diffusion of B atoms occurs from regions of high activity to regions of low activity, these minima yield funnels in their neighborhood, channeling solute atoms toward the tips. This channeling effect implies that regions close to the core of the inclusion receive less solute atoms, in agreement with the observations. Figure 16 can thus be understood as follows: (i) in the early stages of growth, perturbations grow by a Mullins-Sekerka mechanism; (ii) once small tips are formed, the channeling effect set in, causing a gradual shift toward a more directed growth mode and the inhibition of the mode instability owing to the increasingly anisotropic solute diffusion; during this intermediate regime, the FRIs decrease; and (iii) finally, at larger sizes, channeling is so efficient that few solute atoms reach the core of the inclusions, thus strongly suppressing mode instability. This also explains why tip splitting is not observed as could have been expected at an unstable interface.

Since this directed growth regime is not observed for homogeneous inclusions, it is probably a by-product of elasticity. In order to evaluate this possibility, we carried out the elastic relaxation of a pure-B inclusion of similar shape as the inclusion shown in Fig. 20 within a pure-A matrix. This enables us to obtain the local elastic energies everywhere in the inclusion. These results are reported in Fig. 21. The similarity with Fig. 20 is striking: activity and elastic energy minima at the tips of the inclusion coincide, showing that the tips grow because they correspond to elastically favored regions where the strain energy is small.

4. Dynamical corrections to the GT relation

Having analyzed the shape evolution occurring during the growth of soft inclusions, we now turn to the study of the consequences of these morphological changes on the coarsening behavior of the inclusions.

The GT curves for the inclusions pictured in Figs. 12–14 are reported in Fig. 22. Considering first the smallest supersaturation ($\Delta c^B=0.1\%$), we see that $\Delta\mu/k_BT$ follows closely

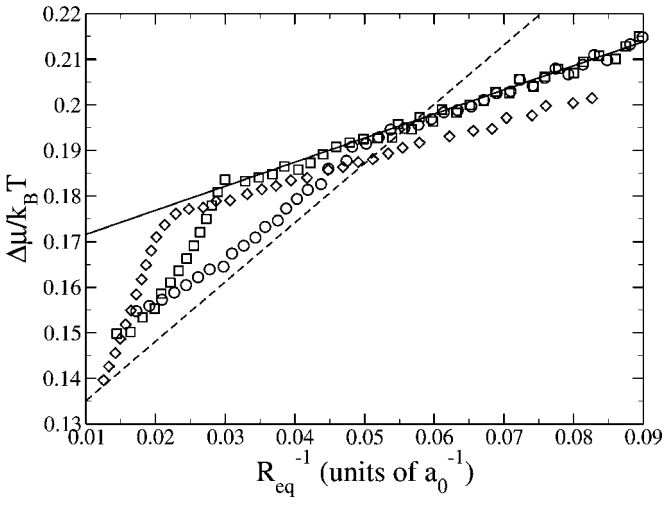

FIG. 22. Dynamical Gibbs-Thomson relations for initially circular soft inclusions: circles: $\Delta c^B=0.1\%$; squares: $\Delta c^B=0.5\%$; diamonds: $\Delta c^B=10\%$. The continuous and dashed lines are fits to the two sections of the equilibrium Gibbs-Thomson relation (c.f. Fig. 11).

the equilibrium behavior at small sizes. Furthermore, the transition toward the elliptic shape occurs near the equilibrium transition point ($R_{eq}^{-1}=0.59a_0^{-1}$, $R_{eq}=17a_0$). However, a small but significant deviation from the equilibrium curve is observed as the size increases. This deviation does not resorb but, on the contrary, increases steadily, signaling the existence of persistent deviations from the equilibrium shape, even at this very low supersaturation.

This is further illustrated by the analysis of the GT curve of the three-branched inclusion depicted in Fig. 13, which corresponds to a slightly higher supersaturation ($\Delta c^B=0.5\%$). Now the transition away from the circular shape begins at about $R^{-1}=0.33a_0^{-1}$ ($R=33a_0$). At this point, the inclusion is already strongly out of equilibrium since it followed the circular branch of the equilibrium GT relation deeply into the elliptic region. The GT curve then drops abruptly. This abrupt change corresponds to the beginning of the very fast amplification of mode 3. A similar behavior is observed for the highest supersaturation ($\Delta c^B=10\%$) except that the shape transition now occurs at a very large radius (around $R=50a_0$). The slope of the GT curves are also different in the large inclusion region, showing that this measurement is very sensitive to the topology of the inclusions. This dynamical GT relation enables us to estimate the extent of the dynamical corrections on the coarsening behavior of the inclusion. The driving forces imposed by the supersaturated matrix are approximately 0.05, 0.13, and 0.67 for $\Delta c^B=0.1\%, 0.5\%$, and 10%, respectively, compared to dynamical corrections of about 0.01–0.03. These results indicate that dynamical effects can significantly alter the coarsening behavior of soft inclusions, particularly at low supersaturation.

The impact of the morphology on the growth dynamics can be quantified more precisely by taking advantage of the sensitivity of the growth process to initial conditions. Using this fact, it is possible to select the number of tips of the growing inclusion and, hence, to study the evolution of inclusions of different shapes in the same environment. The result of such calculation is shown in Fig. 23, where the evolution of the ratio of the areas of inclusions of different shapes to that of a twofold symmetric one is reported. The data show that the difference of area between inclusions of different shapes is of the order of 10% for $\Delta c^B=0.5\%$ in the range of sizes probed here, in agreement with the rough estimate provided above. These effects could even be stronger for smaller supersaturations and larger inclusions, typical of the later stages of coarsening, since the FRIs will be higher in this case.

This example clearly shows that the coarsening rate of a soft inclusion is quite sensitive to its shape. Since the shape is also unstable against small changes in growth conditions, the equilibrium GT relation alone does not provide an adequate account of the growth dynamics, even in an idealized environment. Thus, in complex configurations typical of realistic microstructures, direct elastic interactions or modulations in the solute concentration field could further affect the shape of the inclusions, and hence strongly modify their growth dynamics. This will be the subject of future investigation.

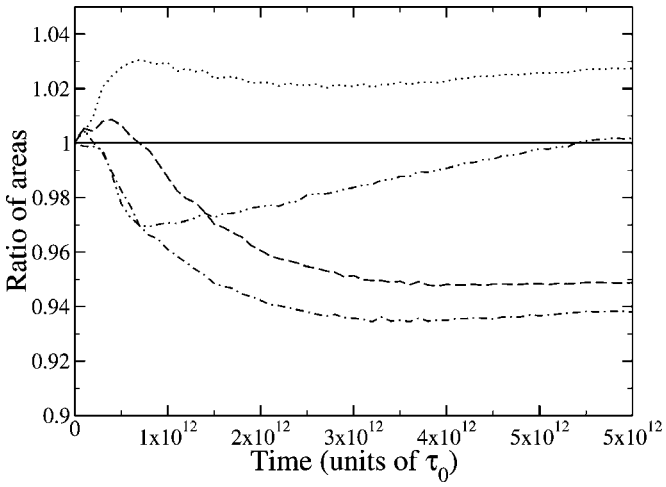

FIG. 23. Ratio of the areas of soft inclusions of different shapes to that of a twofold symmetric inclusion for $\Delta c^B=0.5\%$: continuous line: twofold symmetric inclusion; dotted line: threefold symmetric inclusion; dashed line: fourfold symmetric inclusion; dash-dotted line: fivefold symmetric inclusion; dashed-dotted-dotted line: sixfold symmetric inclusion.

IV. DISCUSSION

From the previous results, it is possible to infer the consequences of elasticity on the coarsening of a collection of inclusions, as long as direct elastic interactions between inclusions remain small compared to inclusion-matrix interactions. In this dilute limit (which also implies quasistatic growth), it is well known that the coarsening behavior of a collection of inclusions is adequately described by the Lifshitz-Slyozov-Wagner (LSW) model of ripening [48]. This model provides an evolution equation for the size distribution $f(t,R)$ of a collection of inclusions interacting diffusively, of the form

$$\frac{\partial f(t,R)}{\partial t}=-\frac{\partial}{\partial R}\left[\frac{dR}{dt}f(t,R)\right], \tag{20}$$

where dR/dt is the rate at which an inclusion of radius R grows. In the context of the LSW model, this rate is given by

$$\frac{dR}{dt}\propto\frac{1}{R}[\mathcal{A}_m-\mathcal{A}_I(R)], \tag{21}$$

where $\mathcal{A}_m$ $[\mathcal{A}_I(R)]$ is the activity inside the matrix [inclusion]. For simplicity, we ignore the presence of vacancies in this derivation, so that a single activity can be used. In this model, the activity of the matrix is taken to be proportional to the solute supersaturation $\Delta(t)$, while the activity of the inclusion follows the Gibbs-Thomson behavior. In order to close the system of equations, we must enforce solute conservation, i.e.,

$$Q_0=\Delta(t)+\int_0^\infty \pi R^2 f(R,t)dR \tag{22}$$

where Q_0 is the initial total supersaturation. Without loss of generality, we adopt the following convention:

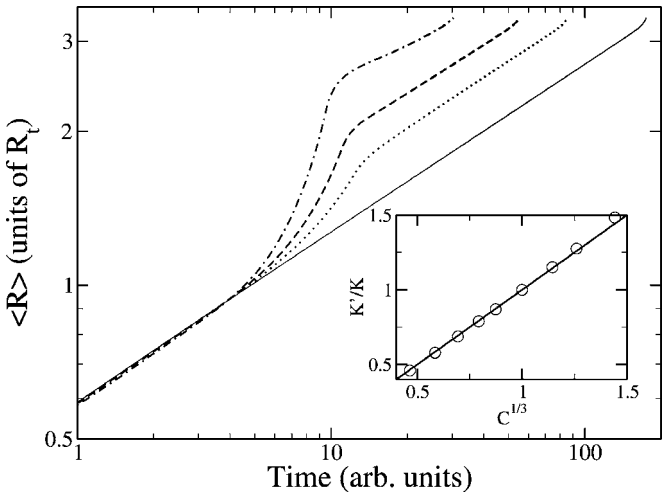

FIG. 24. Time evolution of the average inclusion size for a LSW model of coarsening with different values of the parameter C (see text): continuous line: $C=1$; dotted line: $C=2$; dashed line: $C=3$; dashed-dotted line: $C=5$. Inset: dependence of the ratio of the prefactors K'/K on the value of C. Symbols: measured values; continuous line: $K'/K=C^{1/3}$.

$$\mathcal{A}_m(t) = \Delta(t) \tag{23}$$

$$\mathcal{A}_i(t) = \frac{(1-C)}{R_t} + \frac{1}{R} \quad \text{if } R \leq R_t \tag{24}$$

$$\frac{C}{R} \quad \text{if } R > R_t, \tag{25}$$

with R_t is the radius at which the shape transition occurs and C is the Gibbs-Thomson prefactor for inclusions larger than R_t.

We numerically carried out the integration of Eq. (20) and computed the average inclusion size as a function of time from $f(R,t)$. The results are presented in Fig. 24 for values of C ranging from 1 to 5. First, for $C=1$, corresponding to either homogeneous or hard inclusions, the usual $\langle R\rangle = Kt^{1/3}$ behavior is obtained, as expected. For $C>1$ (soft inclusions), two different regimes are observed. First, at low radius, the normal $\langle R\rangle = Kt^{1/3}$ is seen, since in this range the Gibbs-Thomson relation is unchanged. On the other hand, for sizes much larger than R_t, a $t^{1/3}$ behavior is also observed, albeit with an increased prefactor K'. This is also expected, since most of the size distribution function is then located in a regime where the activity is again proportional to $1/R$. These two regimes are connected by a crossover region whose width is related to the width of $f(R,t)$. The inset of Fig. 24 shows that the prefactor in the large inclusion regime is given by$K'/K=C^{1/3}$. Thus, our calculations show that, at low volume fraction, elastic effects will not affect the scaling exponent of the average size versus time but instead will slightly modify the prefactor. These findings corroborate the results and analysis of Thornton *et al.* [49] concerning the coarsening behavior of a system of inclusions with homogeneous and anisotropic elasticity, where a similar shape transition is also observed.

In the above calculations, it was assumed that inclusions are in their equilibrium configuration relative to their size. However, as the volume fraction increases, larger chemical potential gradients would be allowed to form, thus increasing growth or evaporation rates of inclusions. In this context, dynamical effects could affect the coarsening behavior in a more profound way. Although homogeneous or hard inclusions were shown to be largely immune to such effects, soft inclusions are much more prone to shape transitions. These transitions in turn affect their coarsening behavior, as shown in the previous section. Although the normal LSW regime will eventually be restored as the supersaturation of the matrix decreases, the duration of the initial transient could potentially be much longer than for homogeneous or hard inclusions. On the other hand, an increase of the volume fraction will eventually lead to direct interactions between inclusions through the strain field. These interactions are known to drastically affect both the morphology of the inclusion and their coarsening rate (see Ref. [1], for a recent review). An analysis of the impact of direct interactions using the TDDFT model is underway.

Note that this analysis did not take into account the possibility of oscillations of the chemical potential as a function of size, as observed for hard inclusions in Fig. 8. A detailed study of the origin of these oscillations and their significance for coarsening will be presented elsewhere [47].

V. CONCLUSION

The results of Sec. III demonstrate that our multiscale TDDFT-based model is able to reproduce known equilibrium and dynamical properties of isolated inclusions and to reveal insights about the role of elasticity in their evolution. Indeed, for elastically homogeneous systems, the classical GT relation for circular inclusions is recovered. Under growth conditions, the observed shape instabilities are in quantitative agreement with the Mullins-Sekerka [5] theory. Our model also enabled us to identify the mechanism via which certain modes are preferentially excited by the discrete atomic lattice. Departure from the predictions of the linear MS model were observed and described. Finally, the impact of the shape perturbations and of solute trapping on the chemical potentials of the inclusions were quantified and shown to be negligible in the conditions we studied.

Turning to hard inclusions, we observed that the circular shape is stable and that the form of the GT relation is not affected by elasticity, as expected. We also observed that elasticity stabilizes hard inclusions against shape perturbations during growth, in agreement with the theory of Leo and Sekerka [6]. The magnitude of the solute trapping correction to the chemical potential is observed to be large compared to the homogeneous case because of the coupling between the strain and concentration fields. However, this coupling proves to be too weak to significantly affect the coarsening rate of the inclusions.

Finally, for soft inclusions, we observed the transition from circular shape at small radius to elliptic shape at larger

radius and showed that the general shape of the GT curve is not affected by this transition, but that its slope changes abruptly at the transition point. Concerning dynamical properties, we observed that the shape of soft inclusions is extremely sensitive to the growth rate, even at very low supersaturation, in quantitative agreement with the model of Leo and Sekerka [6]. Strongly out-of-equilibrium shapes are shown to initially form by a mode instability mechanism and to grow by an elastically induced tip-growing mechanism. The dynamical GT relations are shown to strongly depend on the shape adopted by the inclusions so that dynamical corrections have non-negligible effects on the growth rate of the inclusions, even at very low supersaturation.

This first application of the TDDFT framework to multiscale calculation of elastically homogeneous and inhomogeneous systems shows that the method produces results that are in good agreement with analytical models and other simulation methods concerning both equilibrium and dynamical quantities. It also serves to illustrate the advantages of the method: the only input is the potential through which atoms interact; scale-dependent effects stemming from the existence of a fundamental length scale (the lattice parameter) are automatically taken into account and the multiscale formulation enables large systems to be treated at a fraction of the cost of Monte Carlo methods, etc. Although the present formulation of TDDFT, even in its multiscale version, cannot compete with macro- or mesoscopic methods to simulate large systems with complex microstructures, it has proven to be a good candidate to bridge the gap between Monte Carlo methods and phase-field models, and to allow the detailed investigation of intermediate-size systems.

ACKNOWLEDGMENTS

The authors thank Ralf Meyer for stimulating discussions. This work has been supported by grants from the Canadian Natural Sciences and Engineering Research Council (NSERC) and Québec's *Fonds Québécois de la Recherche sur la Nature et les Technologies* (FQRNT). We are indebted to the *Réseau Québécois de Calcul Haute Performance* (RQCHP) for generous allocations of computer resources.

[1] P. Fratzl, O. Penrose, and J. L. Lebowitz, J. Stat. Phys. **95**, 1429 (1999).
[2] W. C. Johnson and J. W. Cahn, Acta Metall. **32**, 1925 (1984).
[3] K. Thornton, N. Akaiwa, and P. Voorhees, Acta Mater. **52**, 1353 (2004).
[4] X. Li, K. Thornton, Q. Nie, P. Voorhees, and J. Lowengrub, Acta Mater. **52**, 5829 (2004).
[5] W. Mullins and R. Sekerka, J. Appl. Phys. **34**, 323 (1963).
[6] P. Leo and R. Sekerka, Acta Metall. **37**, 3139 (1989).
[7] L. Brush and R. Sekerka, J. Cryst. Growth **96**, 419 (1989).
[8] E. Yokoyama and R. Sekerka, J. Cryst. Growth **125**, 389 (1992).
[9] T. Uehara and R. Sekerka, J. Cryst. Growth **254**, 251 (2003).
[10] D. Reinel and W. Dieterich, J. Chem. Phys. **104**, 5234 (1996).
[11] H. Fischer, J. Reinhard, W. Dieterich, J. Gouyet, P. Maass, A. Majhofer, and D. Reinel, J. Chem. Phys. **108**, 3028 (1998).
[12] P. Voorhees, G. McFadden, and G. Johnson, Acta Metall. Mater. **40**, 2979 (1992).
[13] H. Jou, P. Leo, and J. Lowengrub, J. Comput. Phys. **131**, 109 (1997).
[14] I. Schmidt, J. Mech. Phys. Solids **45**, 1521 (1997).
[15] Y. Wang and A. Khachaturyan, Acta Metall. Mater. **43**, 1837 (1995).
[16] A. Onuki and A. Furukawa, Phys. Rev. Lett. **86**, 452 (2001).
[17] J. Zhu, L. Chen, and J. Shen, Modell. Simul. Mater. Sci. Eng. **9**, 499 (2001).
[18] J. K. Lee, Scr. Metall. Mater. **32**, 564 (1994).
[19] J. Lee, Mater. Trans., JIM **39**, 114 (1998).
[20] P. Fratzl and O. Penrose, Acta Metall. Mater. **43**, 2921 (1995).
[21] H. Gupta, R. Winkamer, P. Fratzl, and J. L. Lebowitz, Acta Mater. **49**, 53 (2001).
[22] K. Thornton, J. Agren, and P. Voorhees, Acta Mater. **51**, 5675 (2003).
[23] L. Q. Chen, Phys. Rev. B **58**, 5266 (1998).
[24] M. Plapp and J. F. Gouyet, Phys. Rev. E **55**, 5321 (1997).
[25] M. Kessler, W. Dieterich, H. L. Frisch, J. F. Gouyet, andP. Maass, Phys. Rev. E **65**, 066112 (2002).
[26] N. Sukumar, Int. J. Numer. Methods Eng. **57**, 1 (2003).
[27] R. Eymard, T. Gallouët, and R. Herbin, IMA J. Numer. Anal. **25**, 750 (2005).
[28] E. B. Tadmor, R. Phillips, and M. Ortiz, Langmuir **12**, 4529 (1996).
[29] R. Miller and E. Tadmor, J. Comput.-Aided Mater. Des. **9**, 203 (2002).
[30] R. Miller, E. Tadmor, R. Phillips, and M. Ortiz, Modell. Simul. Mater. Sci. Eng. **6**, 607 (1998).
[31] E. Tadmor, R. Miller, R. Phillips, and M. Ortiz, J. Mater. Res. **14**, 2233 (1999).
[32] P. Zhang, Y. Huang, H. Gao, and K. C. Hwang, J. Appl. Mech. **69**, 454 (2002).
[33] T. Mura, *Micromechanics of Defects in Solids*, 2nd edition (Kluwer, Dordrecht, 1987).
[34] C. Gear, in *Proceedings IFIP 68* (North-Holland, Amsterdam, 1968), pp. 187–193.
[35] P. Brown and Y. Saad, SIAM (Soc. Ind. Appl. Math.) J. Sci. Stat. Comput. **11**, 450 (1990).
[36] H. van der Vorst, SIAM (Soc. Ind. Appl. Math.) J. Sci. Stat. Comput. **13**, 631 (1992).
[37] M. Hestenes and E. Stiefel, J. Res. Natl. Bur. Stand. **49**, 409 (1952).
[38] Y. Yoo, D. Yoon, and M. Henry, Met. Mater. (Soeul, Rep. Korea) **1**, 47 (1995).
[39] M. J. Aziz, J. Y. Tsao, M. O. Thompson, P. S. Peercy, and C. W. White, Phys. Rev. Lett. **56**, 2489 (1986).
[40] A. A. Wheeler, W. J. Boettinger, and G. B. McFadden, Phys. Rev. E **47**, 1893 (1993).
[41] K. Lücke and K. Deter, Acta Metall. **5**, 628 (1957).
[42] M. Hillert, Acta Mater. **47**, 4481 (1999).

[43] J. Langer and R. Sekerka, Acta Metall. **23**, 1225 (1975).
[44] J. Eshelby, Proc. R. Soc. London, Ser. A **241**, 376 (1957).
[45] P. Sharma and S. Ganti, J. Appl. Mech. **71**, 663 (2004).
[46] K. Thornton, N. Akaiwa, and P. Voorhees, Acta Mater. **52**, 1365 (2004).
[47] D. Perez and L. J. Lewis (unpublished).
[48] I. Lifshitz and V. Slyozov, J. Phys. Chem. Solids **19**, 35 (1961).
[49] K. Thornton, N. Akaiwa, and P. W. Voorhees, Phys. Rev. Lett. **86**, 1259 (2001).